Title: Neurovascular coupling actively regulates context-dependent emotional adjustment

Authors: Jiayu Ruan[1,2,3,4], Xinghua Quan[2,3,4], Huiqi Xie[1,2,3,4], Yiyi Zhang[1,2,3,4], Dongdong Zhang[2,3,4], Wentao Wang[2,3,4], Bingrui Zhao[2,3,4], Danping Lu[2,3,4], Jie-Min Jia[2,3,4*]

Affiliations:

1. College of Life Sciences, Zhejiang University, Hangzhou, Zhejiang 310058, China.
2. Westlake Laboratory of Life Sciences and Biomedicine, Hangzhou 310024, China.
3. Key Laboratory of Growth Regulation and Translational Research of Zhejiang Province, School of Life Sciences, Westlake University, Hangzhou 310024, China.
4. Laboratory of Neurovascular Biology, Institute of Basic Medical Sciences, Westlake Institute for Advanced Study, Hangzhou 310024, China.

*Corresponding author. Email: Jie-Min Jia (jiajiemin@westlake.edu.cn)

Abstract:

The ability to flexibly regulate emotions in a contextually appropriate manner is essential for individuals to adapt to varying social stresses, and companion inflexibility involves psychiatric diseases. The extent of this flexibility can possibly be quantified by measuring neurovascular coupling (NVC)-based hemodynamics signal through functional brain imaging. However, whether NVC, in turn, plays an active role in emotion regulation remains unclear due to the absence of exclusive strategies for bidirectionally manipulating NVC. Here, by establishing fifteen genetic mouse models to suppress or enhance NVC, we demonstrated that NVC is an allostatic component required for shaping emotion regulation flexibility. With NVC deficits, the same individual mice simultaneously exhibited being overwhelmed (hyper-response) and suppressing emotions (hypo-response), depending on different contexts. Mechanistically, such opposite effects were likely attributed to NVC oppositely regulating neural activity in the basal lateral amygdala (BLA), a central emotional regulation hub. Importantly, local NVC deficit in BLA leads to hyper-response, which was attenuated by neural chemogenetic antagonization in the BLA. More importantly, enhancing NVC alleviated emotional changes induced by acute and chronic restraint stress (ARS and CRS), highlighting the potential of NVC as a unique therapeutic target that could be able to avoid directly acting on neurons. These findings indicate the active role of NVC in the bidirectional modulation of emotion regulation to fit varying contexts appropriately, emphasizing the necessity of proper NVC for maintaining the homeostasis of advanced brain functions.

Main Text:

The flexibility of emotion control, which may be quantitatively measured by functional brain imaging techniques that detect changes in regional cerebral blood flow (rCBF), is essential to survive in varying environmental stresses that produce rapidly changing contextual demands *(1, 2)*. Enhancing flexibility, such as by acceptance and commitment therapy (ACT), benefits psychological and physical health *(3-5)*. Impaired flexibility is often associated with abnormal neurovascular coupling (NVC) and leads to hypo- or hyper-reactions termed emotion inflexibility, which links diverse psychiatric diseases and even physical well-being *(1, 4)*. For instance, emotional inflexibility, resulting from acute or chronic stresses, is a risk factor for mental health problems such as anxiety, depression, panic disorders, hypervigilance, and agoraphobia *(6)*. These problems sometimes cause physical health problems such as bowel movement problem like chronic pain and constipation (4, 7). Functional magnetic resonance imaging (fMRI) studies have documented a tight spatiotemporal correlation between rCBF and emotion-mirrored neural activities, belonging to the concept of NVC *(8, 9):* under the contexts of innate fear or fear-related post-traumatic stress disorder (PTSD), a profound increase in blood-oxygen-level-dependent (BOLD) signal is always observed in the amygdala, a neural hub that has a central role in the regulation of emotions cross species *(10-13)*. However, whether NVC plays an active role in emotion regulations rather than being a passive measurable parameter remains poorly understood. Therefore, understanding this question may provide a potential therapeutic target that targets vascular cells to regulate emotions and avoids direct actions on neurons, frequently resulting in unwanted severe side effects *(14-16).*

NVC dysfunction is thought to involve many diseases ranging from neurological to psychological conditions *(11, 13, 17, 18)*. However, determining the definitive role of NVC in brain functions remained largely experimentally intractable despite NVC being discovered for more than a century *(19, 20)*. Conventional pharmacological interventions to acutely alter NVC, such as broadly active NO synthase (NOS) inhibitors and PGE2 synthase COX2 inhibitors to suppress the synthesis of vasodilatory substances, introduce insuperable confounds through initial actions beyond the direct inhibiting NVC and thus lack the cell-type specificity and necessary precision. Available nonspecific genetic interventions by depleting $COX2^{-/-}$ *(21)*, $eNOS^{-/-}$ *(22)*, $nNOS^{-/-}$ *(23)*, and potassium channel subunit $KCNJ8^{-/-}$ to suppress NVC chronically. They are also well known to induce severe renal pathology *(24)*, hypertension *(25)*, numerous neural circuit changes *(26-28)*, and vascular arterial smooth muscle cell (aSMC) development deficits *(29)* that would be unwanted in this context, giving rise to multiple direct confounds for the question explored here. Recently, more specific interventions such as endothelial cell (EC)-specific conditional knockout (cKO) of NMDA receptor subunit GluN1 (eNMDAR cKO) and arteriolar EC-specific aEC-Cav1 cKO have been newly developed *(22, 30)*. These may satisfy the question here, but their effects on emotional regulation remain unexplored. In addition, the role of eNMDAR on blood-brain barrier (BBB) integrity should be first evaluated because the damage of BBB integrity in response to stress emerges as a new mechanism to adjust emotional responses *(31-33)*. On the other hand, explicitly enhancing NVC is a critical, independent aspect of evaluating the question, but to our knowledge, no such genetic models are available. Studying the critical question of how NVC actively regulates emotional states has remained inaccessible, and the effect on behaviour still needs to be discovered.

Previously, we have established a synaptic-like transmission mechanism for NVC, a discovery based on the finding of the neuron-smooth muscular junction (NsMJ) *(34)*. We are now exploring the potential of bidirectional NVC interventions by manipulating cation- and anion-permeable neurotransmitter receptors exclusively at NsMJ, the neurovascular communication interface. We could offer potential interventions to avoid unwanted common side effects of mood

stabilizers on neural circuits. These models would enable long-sought functional studies of the physiology of NVC and reveal the active influences on high-order brain functions.

A variety of genetic models that bidirectional regulate NVC

We first generated fifteen cell-type-specific mouse lines (including corresponding controls) using three different promotors (*SMA-creER*, *Pdgfrβ-creER*, and *Emx1-cre*) across two cell types in the neurovascular unit NVU: mural cells and neurons (Fig. 1A). Their effects on NVC were confirmed through a same examination procedure by measuring the functional hyperemia in the barrel cortex with LSCI during the whisker stimulation (Fig.1B) (Fig. 1B). These lines were designed to actively alter NVC using three independent components of NVU: ①blocking NsMJ (26) (*SMA-creER:Grin1$^{f/f}$*, *SMA-creER:Grin2d$^{f/f}$*, *SMA-creER:Grin1$^{f/f}$:Grin2d$^{f/f}$*, *Pdgfrβ-creER:Grin2d$^{f/f}$*, *Pdgfrβ-creER:Grin2d$^{f/f}$:Glrb$^{f/f}$*, *Pdgfrβ-creER:Glrb$^{f/f}$*); ②narrowing down traditional study on total COX2 null mutant (15), encoded by gene *Ptsg2*, to neuron-specific (*Emx1-cre:Ptgs2$^{f/f}$*) and aSMC-specific cKO models (*SMA-creER:Ptsg2$^{f/f}$*); ③directly disrupt contractility of mural cells (*Pdgfrβ-creER:Acta2$^{f/f}$*) (Fig. 1A) *(35)*. If these three categories of models truly converged to reveal a similar effect of NVC on emotion-related emotional changes, it would strongly support that is the case.

To examine which subunits assemble with GluN1 to form functional NMDAR in NsMJ *(34)*, we used RT-PCR to detect all NMDAR subunits in sorted parenchymal aSMCs, using cerebellum as a positive control. We found that *Grin2d* (gene name of GluN2D) was the only non-core subunit detected (Fig. 1C and D). RNAscope further confirmed that *Grin2d* puncta appeared in aSMCs of *SMA-creER:Ai14* brain slices (fig. 1E). The specificity of RNAscope probes was strictly validated in young and adult cerebellum, wherein *Grin2d* is known to show an opposite temporal expression trajectory to *Grin1 (36)* (fig. S1A and B). The GluN2D antibody was evaluated by detecting robust signals in the postnatal day 0 (P0) cerebellum, extremely low in neural stem cell promotor (*Nestin-cre*)-driven cKO cerebellum at the same age, and adult cerebellum, where GluN2D is known as barely expressed *(37)* (fig. S1C). Similar to RNAscope data, GluN2D was found clustered in aSMCs, while it was almost absent in *Grin2d^{cKO}* cells (Fig. 1F and G). These imaging data were further confirmed by biochemistry elevations *in vitro* (Fig. 1H). Importantly, this absence of GluN2D in the cKO group caused no interruptions for neuronal GluN2D expression (Fig. 1I), which proved the cell-type specificity of *SMA-creER* (Also can be seen in fig. S14B). Besides, the basal level of contractile proteins (smoothelin and a-SMA) in the cKO group did not change, implying basal contraction ability was unaffected (fig. S1D and E). Like GluN1 *(34)*, GluN2D was merely found in aSMCs in peripheral organs, excluding the potential impacts on peripheral systems (fig. S2). Except for specificity inspection, we excluded the possibility of the side effects of tamoxifen and long-term stimulations on whisker stimulation-induced hemodynamic increase (fig. S3). All these examinations indicated that we neither directly altered neural circuits nor caused any functional defects in aSMCs, which is particularly important.

Next, we embarked on evaluating NVC for those tamoxifen-induced cKO lines. First of all, singly *SMA-creER:Grin1$^{f/f}$* and Singly *SMA-creER:Grin2d$^{f/f}$* produced a similar degree of NVC reduction as that was produced by singly *Pdgfrβ-creER:Grin2d$^{f/f}$* and doubly *SMA-creER:Grin2d$^{f/f}$:Grin1$^{f/f}$* (Fig. 1J). This again functionally supported GluN2D the only subunit assembled with GluN1 in aSMCs and confirming the role of glutamatergic-NsMJ in NVC *(34)*. Secondly, *Emx1-cre:Ptgs2$^{f/f}$* with molecular validations (fig. S4A-C) exhibited robust reduction in NVC (Fig. 1J) to the level of null mutant *(21)*. Although *Ptgs2* can be detected in aSMC (fig. S4D) with the protein level confirmed *(38-40)* (fig. S4E), *SMA-creER:Ptgs2$^{f/f}$* showed comparable NVC as controls (Fig. 1J), indicating that neurons and aSMC likely used different COX2 signalling

pathways to mediate NVC. Thirdly, the half reduction of α-SMA, a contractile protein encoded by gene *Acta2*, through *Pdgfrβ-creER:Acta2*$^{f/f}$ in mural cells profoundly dampened NVC (Fig. 1J and K). In brief, compared with previous work, we established different cell-type specifically genetic models that suppressed NVC from three independent components of NVU.

Lastly and notably, we successfully established an NVC-upregulation genetic model. Considering that disrupting a cation channel as NMDAR in NsMJ suppresses NVC *(34)* (Fig. 1J), we assumed that disrupting anion channels might enhance NVC. According to past brain SMC transcriptomic studies detected ligand-gating chloride channels, for instance, glycine receptor subunit b (GlyRβ, encoded by gene *Glrb*) (fig. S4F) *(38, 39)* showed relative high expression in venular SMCs (vSMCs). We confirmed *Glrb* puncta and protein clusters with more frequency found in vSMCs than aSMCs (Fig. 1L-O). We further identified GlyRβ colocalizing with gephyrin *in vitro* (Fig. 1R and S), a scaffold protein often segregated in inhibitory postsynaptic sites *(41)*, suggesting that GlyRβ could be clustered on the postjunctional membrane of glycinergic NsMJ. This speculation was further supported by the finding that frequent direct contact of neural axons onto venular SMCs (Fig. 1T). We effectively knocked *Glrb* out specifically in mural cells using *Pdgfrβ-creER:Glrb*$^{f/f}$ (Fig. 1N, P, and Q) and whisker stimulation assay revealed that *Pdgfrβ-creER:Glrb*$^{f/f}$ line enhanced NVC by 16.84 %, approximately 37.25% higher than averaging from six kinds of controls (Fig. 1J). These data together supported the viewpoint that glycinergic NsMJ suppresses NVC at basal homeostasis condition and removal of it leads to enhanced NVC. We predicted that double knockout of *Grin2d* and *Glrb* would neutralize the effects of single cKO on NVC. Indeed, we found no changes in NVC in *Pdgfrb-creER:Grin2d*$^{f/f}$*:Glrb*$^{f/f}$ mice (Fig. 1J), not only providing a stricter control than usual single *Grin2d*$^{f/f}$ or *Glrb*$^{f/f}$ mice but also suggesting that two independent pathways could antagonize with each other.

Taking it all together, we have generated genetic models of bidirectional alterations in NVC with cell-type specificity that crossed multiple NVU enterprise components: neurons, mural cells, and NsMJ. With such a variety of genetic tools, we could approach the long-standing question of whether NVC actively regulates emotional responses.

NVC is required to shape the capacity of flexible emotion regulation

Prior to determining whether NVC-deficient mice exhibit an abnormal emotional responses, we first use *SMA-creER:Grin2d*$^{f/f}$ and its control as an example to examine overall physiological features under the home cage context where there would be the minor stress level. All features were comparable between the two lines, including food consumption, water intake, defecation, urination, body weight, blood pressure, and colorectal health inspection (fig. S5A-N). Importantly, *SMA-creER:Grin2d*$^{f/f}$ did not show BBB leakage (fig. S5O and P). All behaviour assays were performed in a strict, double-blind manner.

Because defecation and urination behaviours have been documented as emotional indices to measure emotional responses in numerous research works regarding anxiety, excitement, or fear-like emotions *(42, 43)*, we included them as examination objectives. Surprisingly, only very mild stress, just by switching mice from the home cage to a regular open field box (40*40 cm^2, shortened as OFT_40*40) for 15 min (Fig. 2A), revealed hyper-response in whichever NVC-downregulation models (Fig. 2B-D).

Specifically, we examined a total of 228 mice, which comprised eight cKO lines and corresponding controls, leaving out *SMA-creER:Grin2d*$^{f/f}$*:Grin1*$^{f/f}$ (Fig. 2B-C). Notably, qualitative analysis of defecation rate, defined as the fraction of total tested mice that defecated at least once, revealed that all lines with NVC deficiency, regardless of neuron-, aSMC- or mural cell-specific lines, exhibited nearly twice as high as control lines (87.5%-100% vs. 50%-64.29%) (Fig. 2B). And the urination rate was generally consistent (fig. S6). Particularly, in two lines with

direct impact on executors of NVC (*Exm1-cre:Ptsg2*$^{f/f}$ and *Pdgfrβ-creER:Acta2*$^{f/f}$), we observed a 100% defecation rate as high as the results from constrictive tube stress (Fig. 2B), suggesting that the NVC deficit may have made a big splash in emotional regulations.

Quantitative analysis consistently revealed that all NVC-deficient lines produced three to four times more total fecal particles than controls (Fig. 2B and C). By contrast, control lines, cKO lines with no NVC deficits (*Pdgfrβ-creER:Grin2d*$^{f/f}$*:Glrb*$^{f/f}$ and *SMA-creER:Ptsg2*$^{f/f}$), and NVC enhancement line (*Pdgfrβ-creER:Grin2d*$^{f/f}$) produced around one fecal particle during 15 min (Fig. 2C). Similarly, feces maximum values also indicated the same conclusion (Fig. 2D). These observations suggest that the basal level NVC is a necessarily allosteric component for the brain to avoid generating overwhelmed emotion status under the context of mild stress, where further enhancing NVC above baseline seemed no more benefits (Fig. 2C). By contrast, enhanced NVC (*Pdgfrβ-creER:Grin2d*$^{f/f}$) robustly suppressed the defecation amount once the context shifted from OFT to tube stress, a much more potent stressor (Fig. 2C). These bidirectional manipulations of NVC suggested that the brain may demand a wide range of NVC capacity to adjust swift emotional responses when switching from context to context.

More detailed examinations further consolidated the observations aforementioned. Using *SMA-creER:Grin2d*$^{f/f}$ mice as an example, they responded strongest during the first 5 min, showing 12 times more feces and then gradually lesser during the following two 5-min periods, 3.5 folds and 3.0 folds, respectively (Fig. 2D). Besides, there was a profoundly shorter latency, referring to the time needed to produce the first feces, in NVC-deficient mice compared to controls (Fig. 2F). Some cKO individuals immediately defecated after entering the arena, which was never observed in controls. There was no difference in the total running distance and the related time-in-centre parameter for measuring anxiety-like levels of these lines in OFT_40*40 (fig. S7). Aforementioned evidence suggested that the defecation-represented emotion was less associated with anxiety under the open-field context.

Surprisingly, the size of OFT with gradually decreasing space revealed a neat, negative correlation with the changes in emotion index (defecation), showing gradually increasing fecal particles (Fig. 2G and H). Normal mice can distinguish the slight difference in spatial sizes among open-filed areas of 40*40 cm^2 (OFT_40*40), 35*35 cm^2 (OFT_35*35), and 16*38 cm^2 (OFT_16*38) (Fig. 2G and H), reflecting the capacity of modulating the intensity of emotions, a hard-core nature of emotion flexibility to adapt to the demands of a given situation. This behaviour paradigm provided an objective method to explicitly exhibit emotion flexibility, often subjectively measured in human studies by addressing questionnaires *(44)*. Notably, disrupted flexibility by defective NVC showing abruptly reaching the plateau (Fig. 2H). This data demonstrated that mice with down-regulated NVC lost the capability of emotion flexibility.

A summary heatmap including two more genetics-independent manipulations (mentioned below) revealed a qualitative correlation: the basal NVC function was linked to the emotion index, the higher NVC function was mirrored with the lower emotional index, and the lower NVC function was associated with the higher emotional index (Fig. 2I).

In mechanism, to identify and then specifically knock down functional protein partners of NMDAR within aSMC cytosol, we performed proteomic analysis after co-immunoprecipitation assay using primary aSMCs with overexpression GluN2D. KEGG analysis of the overlapped 75 proteins that were repeatedly identified in three separate independent experiments revealed that the pathway of *vascular smooth muscle cell contraction* was enriched (fig. S8A). Among proteins in this pathway, caldesmon, a calmodulin-binding protein crucial for SMC contraction and relaxation *(45)*, was further confirmed to interact with GluN2D by Western blotting (fig. S8B). Due to the specific expression patterns of caldesmon in mural cells, knocking down caldesmon by cistern magna injection of *Cald* (gene name of caldesmon) siRNA led to NVC downregulation as

well as hyper defecation (fig. S8C-I). The aforementioned evidence suggested that mechanistically, caldesmon may be the downstream protein of GluN2D in aSMCs for NVC regulation.

Previous studies have found that subjecting mice to an eight-week high-fat diet (HFD) led to deficits in neurovascular coupling (NVC) and blood-brain barrier (BBB) leakage *(17, 46, 47)*. However, whether BBB leakage is the primary cause of NVC deficits is still uncertain. Additionally, if the HFD in humans also results in NVC deficits and emotional inflexibility, an applicable connection between this study and clinical therapy could be established. To clear the relationship between NVC deficits and BBB leakage, we shorted the HFD challenge to four weeks. A robust increase in body weight (fig. S9A) can be seen, leading to hyper defecation despite mice tending to eat less food in the HFD group (fig. S9B). Importantly, we found that at four weeks, BBB seemed still intact when NVC was dampened (fig. S9C and D), demonstrating NVC deficits and emotional inflexibility occurring earlier than BBB breakage. We found that NVC-deficit can be seen in the HFD group (fig. S9E and F), companied by increased defecation in OFT_40*40 (Fig. 2J) but decreased defecation in the home cage (fig. S9G). This result raised a stronger temporal association between NVC and emotional changes, providing a potential treatment for high Body Mass Index (BMI) individuals with emotional inflexibility.

Given that several reviews have suggested that NVC is one of the critical factors in neurological diseases, especially Alzheimer's disease *(48)*, we compared 18-month-old *SMA-creER:Grin1*$^{f/f}$ mice with 5XFAD mice. No apparent Amyloid-β plaque was developed in chronic NVC-deficient mice (fig. S10). This suggested that a single factor of NVC dysfunction alone cannot induce neurological diseases.

In summary, three effects on NVC (upregulated, unchanged, downregulated) observed in these models revealed a negative correlation between the NVC function and the capacity for emotional regulation. This versatility has likely ruled out other contributions of side effects but the indispensable NVC deficit. Taking all results together, we claim that NVC primarily adjusts emotional responses that fit stress levels appropriately.

NVC-deficient mice exhibit decreased fear-like behaviors

We continued to use *SMA-creER:Grin2d*$^{f/f}$ mice as NVC-deficit model to evaluate the universality of the NVC function in emotion regulation beyond the context of switching to a new locomotion environment, such as innate fear of insecure places, innate fear of predators, and social fear of aggressors. Prey mice are believed to feel emotionally and naturally more fearful on white floors and more secure on black floors *(49)*. We separated a chamber with a metal fence into the left with a white floor and the right with a black floor (Fig. 3A). We placed one mouse at a time into the white side. This design allowed the mouse to see through but not be able to cross the fence to get into the darker side so that the travelling time spent and active approaches near the dark side may be used as emotion index of innate fearful-like emotional response to the white side (Fig. 3A). We have named this assessment the "open-field-like test" (OFLT) in this study. Control mice displayed an expected innate fear-like response as evidenced by their longer travel time near the dark side (Fig. 3B-D), longer time to approach the dark side by exhibiting more times of sniffing and climbing the fence (fig. S11A and B). Although NVC-deficient mice could cognitively recognize which side was insecure, they exhibited a much lower-level preference to the dark side, implicating lower innate fear-like status while staying in an insecure place (Fig. 3B-D). Interestingly, hyper-defecation behaviour was again observed under the OFLT context (fig. S11C). Given that hyper-defecation may represent higher levels of anxiety, fear, and excitement, what NVC-deficient mice exhibited should belong to hyper-excitement because they had a lower level of fear-like emotion compared to normal mice shown above. Secondly, higher total running distance (fig. S11D), a typical hyperactivity phenotype induced by psychostimulants such as morphine *(50)*. Thus, in a

more complex context like the OFLT than OFT, individual mice may simultaneously exhibit decreased innate fear-like emotion and oppositely increased hyper-excitation-like emotion.

Shortened subsiding process after predator-like threats stimulation in NVC-deficient mice

To systemically evaluate the level of innate fear in the NVC-deficient model, mice undergo three threatening paradigms: a movie showing an approaching cat, classic looming stimulation mimicking predator diving, and virtual reality of eagle hunting (shortened as Cat_{movie}, looming, and VR_{eagle}, respectively) (Fig. 3E-Y).

First, we recorded the behavioural responses of awake, head-fixed mice on a treadmill repeatedly stimulated by Cat_{movie} with three trials (Fig. 3E and Movie. S1). As expected, in response to the first trial, control mice showed the most retreat and tail rattling, typical defensive behaviours when experiencing innate fear (Fig. 3F). This demonstrated Cat_{movie} was an effective stimulus. Notably, most NVC-deficient mice exhibited no retreat behaviour at all (Fig. 3G). Even among the rest small subset of this group, the intensity of defensive behaviours was also remarkably reduced (Fig. 3H-J). These observations of defensive responses suggest a lower level of innate fear-like status in NVC-deficient mice, supporting the findings from OFLT (Fig. 3A-D).

Next, to enhance the observation by the Cat_{movie}, we stimulated free-moving instead of head-fixed mice with looming (Fig. 3K). Mice would not receive stimulation until they reached a moving speed of 13-15 cm/s (Fig. 3L) before the stimulation. No differences in locomotion speed can be detected between NVC-deficient mice and their controls before the stimulation (fig. S12A). The looming constantly induced consistent freezing behaviour of both genotypes, showing the reduction of locomotion speed down to 1-2 cm/s shortly after the initiation of stimulation. This observation demonstrated that NVC-deficient mice had normal visual sensation and cognitive understanding of looming threats (Fig. 3L). Notably, the heatmap profile, showing the locomotion speed of all mice for each group, revealed that NVC-deficient mice exhibited shorter subsiding than controls (Fig. 3M). Other behavioural characterizations including shorter latency recovery from freezing status (Fig. 3N) and lower rearing index observed in NVC-deficient mice. Altogether, again, it reflected a lower innate fear-like status like in OFLT (Fig. 3E-J).

Lastly, we updated looming system to VR_{eagle} system to threaten mice by delivering an eagle-hunting video played in a ballroom to make more realistic environment (Fig. 3P). As the nonvoluntary change of pupil size serves as an objective measurement for innate fear status *(51)* and the locomotion speed is an index often used across many studies *(52)*, we recorded these two parameters simultaneously from awake, head-fixed mice placed on a floating ball (Fig. 3P and Movie. S2). Under basal level, pupil size and locomotion speed between two genotypic were not different (fig. S12B and C). Similarly, VR_{eagle} was not provided until mice started to move. VR_{eagle} successfully frightened both genotypic mice by showing a similar abrupt rise in pupil size (fig. S12D), mirrored by a sudden decrease in locomotion speed (Fig. 3Q), again reflecting unchanged cognitive recognition of threats. Based on the aforementioned data, we normalized the locomotion speed at 0s and the pupil size at 3s (Fig. 3Q), and we used the intersection point of normalized locomotion speed and normalized pupil size (shown by the arrow in Fig. 3Q) as the response index to reflect the subsiding extend. It can be seen that NVC-deficient mice exhibited a lower response index compared with controls (Fig. 3R). Besides, we also examined the subsiding process following imminent fear by measuring the latency of recovering these two parameters (for looming assay used locomotion speed, and for VR_{eagle} assay used pupil size) back to the initial basal level (Fig. 3S) in looming assay and VR_{eagle} assay. To our great surprise, two independent assays revealed a very close fold change in the subsiding duration (Fig. 3S), strongly suggesting that NVC deficiency makes animals recover faster from predator threats.

Collectively, all these paradigms were repeatedly applied for three trials (Cat_{movie} and looming) or five trials (VR_{eagle}), and most mice show a general adaptation (fig. S13). Importantly, independent paradigms (looming and VR_{eagle}) commonly revealed a shared feature, and this significant finding that NVC deficit lowered the level of innate fear-like emotion underscores the importance of our research in understanding fear responses in mice.

NVC-deficient mice are less threatened by a real social aggressor

In addition to virtual stressors, we continued to examine emotion regulation under real threats from cohabitating in the same cage with social aggressor CD1 mice. This cage was partly separated into small and large subregions due to the dented metal top so that the two mice were able to travel between them freely (Fig. 3T). Due to naturally fear, the control and NVC-deficient mice tended to avoid CD1 by keeping distance, we predicted that NVC-deficient mice would show less avoidance. Indeed, under the condition that the sniffing recognition process between CD1 and both genotypes of mice was not different (fig.3U), the quantification of the total time when two mice cohabited in the small subregion revealed that the NVC-deficient mice exhibited a longer time (Fig. 3V light color), and so exhibited the total time that recorded which genotype mice took the active entrance into the small region when CD1 had been there (Fig. 3U deep color), indicating that NVC-deficient mice might have a lower intention to avoid aggressive CD1 mice. More strikingly, 98% of control mice fled away from CD1 after fights, and so did only 37% of NVC-deficient mice (Fig. 3W left). Consistent with the mice flee rate, we normalized it to total fight events. There were 37 and 19 fights between the 8 controls with CD1 and 10 NVC-deficient mice with CD1, respectively, among which CD1 actively triggered the most fights. NVC-deficent mice exhibited significant smaller percentage of flee rate than controls (Fig. 3W right). These observations strongly supported that even under the context of real stressors, NVC modulated internal emotional status, highlighting that NVC deficit disrupted fear emotion processing.

NVC actively modulates context-dependent emotion flexibility through differently tuning BLA neural activity

We focused on the well-known brain nucleus, the amygdala, to delineate the mechanism underlying how NVC regulates emotions. We hypothesize that NVC deficiency differentially alters amygdala activity in a context-dependent manner. So, we profiled the expression patterns in the basal lateral amygdala (BLA) of early response gene c-Fos expressions across the aforementioned seven paradigms, shown as heatmaps (Fig. 4A). As expected and consistent with previous reports *(53)*, compared to the home cage, the rest six paradigms all increased c-Fos expressions, but their levels and location patterns varied from context to context (Fig. 4A). We generated a pattern similarity index by a double-blinded data-analysis specialist (see the Method) to conduct an unbiased cluster analysis to see whether the c-Fos expression patterns can represent the corresponding paradigms. Notably, among the seven paradigms, the similarity index between the most similar two paradigms of looming and VR_{eagle} ranked the top one and ranked top two between the home cage and OFT_40*40. This analysis demonstrated that the similarity index was a reliable indicator, and this index also suggested that VR_{eagle} is a reliable and updated behavioural assay born out of the looming assay. Thus, we considered that NVC could differentially alter BLA neural activity in a context-dependent way. Apparently, *SMA-creER:Grin2d*$^{f/f}$ exhibited disrupted BLA activation patterns across contexts (Fig. 4A bottom panel), which may be the basis of abnormal behaviour.

We chose the series of OFT and predator threats as exemplary paradigms for deeper investigations. Within this pool of five contexts, the similarity classification unbiasedly grouped the home cage and two OFT assays into one class while grouped looming and VR_{eagle} into the other

class (Fig. 4B). In contrast, this classification messed up in NVC-deficient mice (Fig. 4B). Furthermore, we found that comparing these two genotypic mice, the higher elevation of c-Fos expression in the BLA (hyperactive BLA) under the OFT context, whereas oppositely lower elevation (hypoactive BLA) in the predator context in *SMA-creER:Grin2d*$^{f/f}$ mice compared to controls (Fig. 4C). It is worthy to mention that this observation was consistently repeated by two independent paradigms for each context (Fig. 4C). When plotting the differences in the emotion-index changes and the differences in the c-Fos-expression changes between the two genotypes in one graph, there seemed to be a positive correlation, that is, hyperactive BLA correlating with hyper-excitement under the OFT contexts and hypoactive BLA correlating with hypo-response under the looming and VR_{eagle} contexts (Fig. 4D). This observation of differentially neural regulations by NVC may mechanistic explain how NVC differently modulate emotion regulations in a context-dependent manner.

If this is the case, we further hypothesise that antagonising neural activity in BLA would reverse the effect of NVC deficiency on emotion regulations. By contrast, locally induced NVC deficiency in BLA could modulate emotion regulations. First, we took the OFT assay as an example to perform chemogenetic inhibition by local injection of AAV2/5-mCaMKIIa-hM4D (Gi)-EGFP-ER2-WPRE-pA virus to antagonise the hyper-active BLA (Fig. 4E and fig. S15A). The intraperitoneal injection of saline or C21, an agonist for chemogenetic receptor (DREAD), causes extra stress thus induced higher basal defecation index (Fig. 4F) than the data shown in earlier OFT assay (Fig. 2C). We first determined the effectiveness of neural inhibition by using regular quarantine and tube stress assays (fig. S15B). With this technique confirmed, we found that suppression of BLA activity attenuated the context-induced over defecation behaviour in both genotypes, suggesting that at least BLA neural activity is required for NVC-dependent emotion regulation (Fig. 4F). Besides, before we locally injected *Cald* siRNA at the same position in BLA, we confirmed that BLA has conservative blood vessels including arterioles (fig. S14). Forty-eight hours after siRNA injection, we observed a similar defecation increase in OFT_40*40 to cistern magna injection of *Cald* (fig. S8I). Gi inhibition and *Cald* siRNA results suggesting that NVC deficiency in BLA is critical for emotion regulation.

Enhanced NVC mice show emotional resistance to chronic restriction stress

Next, to link our study to clinical application, we aimed to determine the role of enhanced NVC in emotion regulation. We chose tube stress as the example context to address this question since prior acute restraint stress (ARS) data showed lower emotion response in NVC-enhanced *pdgfrβ-creER:Glrb*$^{f/f}$ model (Fig.2B and C). Therefore, we continued to embark on 2-hour tube stress every day for 28 consecutive days to achieve the chronic restriction stress (CRS) model (See the Method), which is believed to eventually lead to depression, anxiety, and mood-dominant constipation *(54-56)*. After validating the effectiveness of the CRS model (Fig. 5A), we found that control mice and *pdgfrβ-creER:Grin2d*$^{f/f}$ mice with CRS exhibited obvious conspiration at the ending day, showing not only apparent fewer feces production but also dryer, less water-containing feces (Fig. 5B-D). Compared with aforementioned data in ARS, NVC deficiency cannot exacerbate or ameliorate restraint stress-induced emotional change. In great contrast, enhanced NVC (*pdgfrβ-creER:Glrb*$^{f/f}$) mice showed robust resistance to both the ARS and CRS by showing normal-trend defecation behaviour and normal quality of feces (Fig. 5C-E), emphasizing that NVC may be a new therapeutic target for mood disorders and its related gastrointestinal problems.

Discussion

In this study, we developed fifteen genetic models with cell-type-specificity plus two cre-independent NVC-deficient models (HFD and *Cald* siRNA), achieving bidirectional regulations

of hemodynamic changes during NVC. These models resulted from single or double perturbations of six protein expressions (GluN1, GluN2D, SMA, GlyRβ, COX2, and caldesmon) within mural cells and neurons of NVU (Fig. 1). We then uncovered that NVC actively regulates emotional/affective behaviours in a context-dependent manner through differently modulating the activity of the emotion centre amygdala. This study implies that active NVC alterations can be critical in causing or ameliorating affective disorders. We propose that NVC can be a new therapeutic target for treating mood-spectrum disorders.

As most gene perturbations in this study were in mural cells, an out layer of vasculature critical for BBB integrity, one may be concerned that there could be side effects independent of NVC playing a more critical role. For instance, BBB leakage and subsequent immune cell infiltration have been documented to have tight associations with affective changes. Through the evens blue leakage inspection, we have preliminarily ruled out this possibility. Besides, the mural-cell-independent model (neuron-specific *Emx1-cre:Pgst2*$^{f/f}$) consistently yielded the same effects (Fig. 1J). Moreover, if it were due to BBB breakage, the *Pdgfrβ-creER:Grin2d*$^{f/f}$*:Glrb*$^{f/f}$ mice, showing no NVC dysfunction, should have exhibited over-defecation behaviours but it did not (Fig. 2B-D). BBB leakage is thought to be the primary reason for HFD-induced cognition declines or emotional changes. However, this study provides that NVC dysfunction could be an alternative primary reason because NVC dysfunction and correlated behavioural changes occur earlier than BBB dysfunction (Fig. 2J and fig. S9). As for other BBB-irrelevant unknown side effects, it would also be improbable because the only overlapped feature of NVC downregulation among the HFD, knockdown of caldesmon and five other independent lines (*SMA-creER:Grin1*$^{f/f}$, *SMA-creER:Grin2d*$^{f/f}$, *Pdgfrβ-creER:Grin2d*$^{f/f}$, *Emx1-cre:Ptgs2*$^{f/f}$, and *Pdgfrβ-creER:Acta2*$^{f/f}$) commonly showed emotional overreactions (Fig. 2I).

A growing body of research in neuroscience, neurology, and psychiatry examines how the diverse NVU cells, beyond the canonical roles in regulating CBF, coordinate and modulate brain activity to regulate cognition and emotion over diverse timescales *(31)*. This study further consolidates this emerging view by demonstrating that NVC, as the prototypic function of NVU cells, actively regulates emotional flexibility. The space size-dependent defection index indicates that emotional flexibility is quantifiable. Our genetic models highlight that NVC is essential for shaping such flexibility based on varying contextual demands, which is demonstrated by the finding that NVC dysfunction leads to the loss of such flexibility (Fig. 2H). Furthermore, it suggested that individuals with impaired NVC may exhibit atypical emotional responses to common stressors.

The cerebral control over emotional flexibility may involve switching neural circuits to achieve the switch of emotional regulatory strategies. Such a neural switch seems regulated by NVC, as the similarity index analyses between environment shift to virtual threats revealed that the same manipulation of NsMJ-based NVC had opposite effects on different subgroups of BLA neurons (Fig. 4A). This may be attributed to different neural circuits that execute different emotion regulatory strategies with different responses to the same incompatible NVC. This could explain how NVC downregulation potentiated emotional overreaction while conversely shortening subsiding after innate fear. Single individuals who have both emotions are widely observed in clinical settings. More interestingly, under CRS, NVC upregulation ameliorated repeated physical constraints-induced anxiety-like behaviours, while NVC downregulation involved neither exacerbation nor amelioration.

To our knowledge, this study, for the first time, developed an NVC upregulated model and demonstrated unprecedented venule-dependent mechanisms underlying NVC. Ultrastructural reconstruction revealed that venular endfeet discontinuity was substantially more significant than capillaries and arterioles. So, we inferred that glycinergic NsMJ was mainly located in venules and

responsible for the NVC upregulation. Previous work mentioned that axon terminals of glycinergic neurons can be seen both in BLA and lateral habenula (LHb), and they are involved in depression regulation *(57)*. Notably, the NVC upregulation model ameliorated the effect on constipation-like symptoms and depression-like emotions induced by CRS, as well as in ARS, resulting in normal-trend emotional index (defecation). This would open a new avenue for studying venule-based NVC to regulate emotions.

In summary, by leveraging these multiple combinations of different genetic models, we have further broadened the research fields of NVC and emotion regulation. Current mood stabilisers are often accompanied by severe side effects on memory or cognitive functions, a significant reason why patients are reluctant to take them. This study suggests an alternative strategy, targeting NsMJ rather than neurons, to avoid unwanted neural side effects.

References and Notes:

1. Roelofs K, Bramson B, Toni I. A neurocognitive theory of flexible emotion control: The role of the lateral frontal pole in emotion regulation. Ann N Y Acad Sci. 2023;1525(1):28-40.

2. Pico-Perez M, Radua J, Steward T, Menchon JM, Soriano-Mas C. Emotion regulation in mood and anxiety disorders: A meta-analysis of fMRI cognitive reappraisal studies. Prog Neuropsychopharmacol Biol Psychiatry. 2017;79(Pt B):96-104.

3. Gould RL, Wetherell JL, Kimona K, Serfaty MA, Jones R, Graham CD, et al. Acceptance and commitment therapy for late-life treatment-resistant generalised anxiety disorder: a feasibility study. Age Ageing. 2021;50(5):1751-61.

4. McCracken LM. Psychological Flexibility, Chronic Pain, and Health. Annu Rev Psychol. 2024;75:601-24.

5. Hayes SC, Wilson KG. Acceptance and commitment therapy: Altering the verbal support for experiential avoidance. Behav Anal. 1994;17(2):289-303.

6. Yao X, Xu X, Chan KL, Chen S, Assink M, Gao S. Associations between psychological inflexibility and mental health problems during the COVID-19 pandemic: A three-level meta-analytic review. J Affect Disord. 2023;320:148-60.

7. Yu Z, Liu LY, Lai YY, Tian ZL, Yang L, Zhang Q, et al. Altered Resting Brain Functions in Patients With Irritable Bowel Syndrome: A Systematic Review. Front Hum Neurosci. 2022;16:851586.

8. Hillman EM. Coupling mechanism and significance of the BOLD signal: a status report. Annu Rev Neurosci. 2014;37:161-81.

9. Iadecola C. Neurovascular regulation in the normal brain and in Alzheimer's disease. Nat Rev Neurosci. 2004;5(5):347-60.

10. Whalen PJ, Kagan J, Cook RG, Davis FC, Kim H, Polis S, et al. Human amygdala responsivity to masked fearful eye whites. Science. 2004;306(5704):2061.

11. Ahmed-Leitao F, Spies G, van den Heuvel L, Seedat S. Hippocampal and amygdala volumes in adults with posttraumatic stress disorder secondary to childhood abuse or maltreatment: A systematic review. Psychiatry Res Neuroimaging. 2016;256:33-43.

12. Harris AP, Lennen RJ, Marshall I, Jansen MA, Pernet CR, Brydges NM, et al. Imaging learned fear circuitry in awake mice using fMRI. Eur J Neurosci. 2015;42(5):2125-34.

13. Kamiya K, Abe O. Imaging of Posttraumatic Stress Disorder. Neuroimaging Clin N Am. 2020;30(1):115-23.

14. Slattery P, Frolich S, Goren I, Nusing RM. Salt supplementation ameliorates developmental kidney defects in COX-2(-/-) mice. Am J Physiol Renal Physiol. 2017;312(6):F1044-F55.

15. Cryan JF, Mombereau C, Vassout A. The tail suspension test as a model for assessing antidepressant activity: review of pharmacological and genetic studies in mice. Neurosci Biobehav Rev. 2005;29(4-5):571-625.

16. Milano J, Rossato MF, Oliveira SM, Drewes C, Machado P, Beck P, et al. Antinociceptive action of 4-methyl-5-trifluoromethyl-5-hydroxy-4, 5-dihydro-1H-pyrazole methyl ester in models of inflammatory pain in mice. Life Sci. 2008;83(21-22):739-46.

17. Huber G, Ogrodnik M, Wenzel J, Stolting I, Huber L, Will O, et al. Telmisartan prevents high-fat diet-induced neurovascular impairments and reduces anxiety-like behavior. J Cereb Blood Flow Metab. 2021;41(9):2356-69.

18. Clemm von Hohenberg C, Weber-Fahr W, Lebhardt P, Ravi N, Braun U, Gass N, et al. Lateral habenula perturbation reduces default-mode network connectivity in a rat model of depression. Transl Psychiatry. 2018;8(1):68.

19. Drew PJ. Neurovascular coupling: motive unknown. Trends Neurosci. 2022;45(11):809-19.

20. Iadecola C. The Neurovascular Unit Coming of Age: A Journey through Neurovascular Coupling in Health and Disease. Neuron. 2017;96(1):17-42.

21. Niwa K, Araki E, Morham SG, Ross ME, Iadecola C. Cyclooxygenase-2 contributes to functional hyperemia in whisker-barrel cortex. J Neurosci. 2000;20(2):763-70.

22. Chow BW, Nunez V, Kaplan L, Granger AJ, Bistrong K, Zucker HL, et al. Caveolae in CNS arterioles mediate neurovascular coupling. Nature. 2020;579(7797):106-10.

23. Yang G, Zhang Y, Ross ME, Iadecola C. Attenuation of activity-induced increases in cerebellar blood flow in mice lacking neuronal nitric oxide synthase. Am J Physiol Heart Circ Physiol. 2003;285(1):H298-304.

24. Morham SG, Langenbach R, Loftin CD, Tiano HF, Vouloumanos N, Jennette JC, et al. Prostaglandin synthase 2 gene disruption causes severe renal pathology in the mouse. Cell. 1995;83(3):473-82.

25. Tsutsui M, Shimokawa H, Otsuji Y, Yanagihara N. Pathophysiological relevance of NO signaling in the cardiovascular system: novel insight from mice lacking all NO synthases. Pharmacol Ther. 2010;128(3):499-508.

26. Pigott BM, Garthwaite J. Nitric Oxide Is Required for L-Type Ca(2+) Channel-Dependent Long-Term Potentiation in the Hippocampus. Front Synaptic Neurosci. 2016;8:17.

27. Kourosh-Arami M, Hosseini N, Mohsenzadegan M, Komaki A, Joghataei MT. Neurophysiologic implications of neuronal nitric oxide synthase. Rev Neurosci. 2020;31(6):617-36.

28. Yui K, Kawasaki Y, Yamada H, Ogawa S. Oxidative Stress and Nitric Oxide in Autism Spectrum Disorder and Other Neuropsychiatric Disorders. CNS Neurol Disord Drug Targets. 2016;15(5):587-96.

29. Ando K, Tong L, Peng D, Vazquez-Liebanas E, Chiyoda H, He L, et al. KCNJ8/ABCC9-containing K-ATP channel modulates brain vascular smooth muscle development and neurovascular coupling. Dev Cell. 2022;57(11):1383-99 e7.

30. Hogan-Cann AD, Lu P, Anderson CM. Endothelial NMDA receptors mediate activity-dependent brain hemodynamic responses in mice. Proc Natl Acad Sci U S A. 2019;116(21):10229-31.

31. Dion-Albert L, Dudek KA, Russo SJ, Campbell M, Menard C. Neurovascular adaptations modulating cognition, mood, and stress responses. Trends Neurosci. 2023;46(4):276-92.

32. Dudek KA, Dion-Albert L, Kaufmann FN, Tuck E, Lebel M, Menard C. Neurobiology of resilience in depression: immune and vascular insights from human and animal studies. Eur J Neurosci. 2021;53(1):183-221.

33. Dion-Albert L, Bandeira Binder L, Daigle B, Hong-Minh A, Lebel M, Menard C. Sex differences in the blood-brain barrier: Implications for mental health. Front Neuroendocrinol. 2022;65:100989.

34. Zhang D, Ruan J, Peng S, Li J, Hu X, Zhang Y, et al. Synaptic-like transmission between neural axons and arteriolar smooth muscle cells drives cerebral neurovascular coupling. Nat Neurosci. 2024;27(2):232-48.

35. Arnoldi R, Hiltbrunner A, Dugina V, Tille JC, Chaponnier C. Smooth muscle actin isoforms: a tug of war between contraction and compliance. Eur J Cell Biol. 2013;92(6-7):187-200.

36. Monyer H, Burnashev N, Laurie DJ, Sakmann B, Seeburg PH. Developmental and regional expression in the rat brain and functional properties of four NMDA receptors. Neuron. 1994;12(3):529-40.

37. Laurie DJ, Bartke I, Schoepfer R, Naujoks K, Seeburg PH. Regional, developmental and interspecies expression of the four NMDAR2 subunits, examined using monoclonal antibodies. Brain Res Mol Brain Res. 1997;51(1-2):23-32.

38. Vanlandewijck M, He L, Mae MA, Andrae J, Ando K, Del Gaudio F, et al. A molecular atlas of cell types and zonation in the brain vasculature. Nature. 2018;554(7693):475-80.

39. Yang AC, Vest RT, Kern F, Lee DP, Agam M, Maat CA, et al. A human brain vascular atlas reveals diverse mediators of Alzheimer's risk. Nature. 2022;603(7903):885-92.

40. Zhang Y, Chen K, Sloan SA, Bennett ML, Scholze AR, O'Keeffe S, et al. An RNA-sequencing transcriptome and splicing database of glia, neurons, and vascular cells of the cerebral cortex. J Neurosci. 2014;34(36):11929-47.

41. Froehner SC. Regulation of ion channel distribution at synapses. Annu Rev Neurosci. 1993;16:347-68.

42. Sarro EC, Sullivan RM, Barr G. Unpredictable neonatal stress enhances adult anxiety and alters amygdala gene expression related to serotonin and GABA. Neuroscience. 2014;258:147-61.

43. Gorard DA, Gomborone JE, Libby GW, Farthing MJ. Intestinal transit in anxiety and depression. Gut. 1996;39(4):551-5.

44. Probst T, Muhlberger A, Kuhner J, Eifert GH, Pieh C, Hackbarth T, et al. Development and Initial Validation of a Brief Questionnaire on the Patients' View of the In-Session Realization of the Six Core Components of Acceptance and Commitment Therapy. Clin Psychol Eur. 2020;2(3):e3115.

45. Janovick JA, Natarajan K, Longo F, Conn PM. Caldesmon: a bifunctional (calmodulin and actin) binding protein which regulates stimulated gonadotropin release. Endocrinology. 1991;129(1):68-74.

46. Chang HC, Tai YT, Cherng YG, Lin JW, Liu SH, Chen TL, et al. Resveratrol attenuates high-fat diet-induced disruption of the blood-brain barrier and protects brain neurons from apoptotic insults. J Agric Food Chem. 2014;62(15):3466-75.

47. Li W, Prakash R, Chawla D, Du W, Didion SP, Filosa JA, et al. Early effects of high-fat diet on neurovascular function and focal ischemic brain injury. Am J Physiol Regul Integr Comp Physiol. 2013;304(11):R1001-8.

48. Park L, Anrather J, Forster C, Kazama K, Carlson GA, Iadecola C. Abeta-induced vascular oxidative stress and attenuation of functional hyperemia in mouse somatosensory cortex. J Cereb Blood Flow Metab. 2004;24(3):334-42.

49. Shoji H, Miyakawa T. Effects of test experience, closed-arm wall color, and illumination level on behavior and plasma corticosterone response in an elevated plus maze in male C57BL/6J mice: a challenge against conventional interpretation of the test. Mol Brain. 2021;14(1):34.

50. Mickley GA, Stevens KE, White GA, Gibbs GL. Endogenous opiates mediate radiogenic behavioral change. Science. 1983;220(4602):1185-7.

51. Wang L, Chen IZ, Lin D. Collateral pathways from the ventromedial hypothalamus mediate defensive behaviors. Neuron. 2015;85(6):1344-58.

52. Shang C, Chen Z, Liu A, Li Y, Zhang J, Qu B, et al. Divergent midbrain circuits orchestrate escape and freezing responses to looming stimuli in mice. Nat Commun. 2018;9(1):1232.

53. Hale MW, Hay-Schmidt A, Mikkelsen JD, Poulsen B, Shekhar A, Lowry CA. Exposure to an open-field arena increases c-Fos expression in a distributed anxiety-related system projecting to the basolateral amygdaloid complex. Neuroscience. 2008;155(3):659-72.

54. Eutamene H, Bradesi S, Larauche M, Theodorou V, Beaufrand C, Ohning G, et al. Guanylate cyclase C-mediated antinociceptive effects of linaclotide in rodent models of visceral pain. Neurogastroenterol Motil. 2010;22(3):312-e84.

55. Lapmanee S, Charoenphandhu J, Teerapornpuntakit J, Krishnamra N, Charoenphandhu N. Agomelatine, venlafaxine, and running exercise effectively prevent anxiety- and depression-like behaviors and memory impairment in restraint stressed rats. PLoS One. 2017;12(11):e0187671.

56. Taguchi R, Shikata K, Furuya Y, Hirakawa T, Ino M, Shin K, et al. Selective corticotropin-releasing factor 1 receptor antagonist E2508 reduces restraint stress-induced defecation and visceral pain in rat models. Psychoneuroendocrinology. 2017;75:110-5.

57. Cui Y, Yang Y, Ni Z, Dong Y, Cai G, Foncelle A, et al. Astroglial Kir4.1 in the lateral habenula drives neuronal bursts in depression. Nature. 2018;554(7692):323-7.

58. Li X, Zhou L, Zhang X, Jin Y, Zhao B, Zhang D, et al. Proteins secreted by brain arteriolar smooth muscle cells are instructive for neural development. Mol Brain. 2022;15(1):97.

59. Yu XD, Zhu Y, Sun QX, Deng F, Wan J, Zheng D, et al. Distinct serotonergic pathways to the amygdala underlie separate behavioral features of anxiety. Nat Neurosci. 2022;25(12):1651-63.

60. Boas DA, Dunn AK. Laser speckle contrast imaging in biomedical optics. J Biomed Opt. 2010;15(1):011109.

61. Jin Y, Shi P, Wang Y, Li J, Zhang J, Zhao X, et al. Precise control of embolic stroke with magnetized red blood cells in mice. Commun Biol. 2022;5(1):136.

62. Liu CY, Chen JB, Liu YY, Zhou XM, Zhang M, Jiang YM, et al. Saikosaponin D exerts antidepressant effect by regulating Homer1-mGluR5 and mTOR signaling in a rat model of chronic unpredictable mild stress. Chin Med. 2022;17(1):60.

63. Guo Z, Li S, Wu J, Zhu X, Zhang Y. Maternal Deprivation Increased Vulnerability to Depression in Adult Rats Through DRD2 Promoter Methylation in the Ventral Tegmental Area. Front Psychiatry. 2022;13:827667.

64. Kim S, Hong KB, Kim S, Suh HJ, Jo K. Creatine and taurine mixtures alleviate depressive-like behaviour in Drosophila melanogaster and mice via regulating Akt and ERK/BDNF pathways. Sci Rep. 2020;10(1):11370.

65. Oh YS, Gao P, Lee KW, Ceglia I, Seo JS, Zhang X, et al. SMARCA3, a chromatin-remodeling factor, is required for p11-dependent antidepressant action. Cell. 2013;152(4):831-43.
66. Seo JS, Park JY, Choi J, Kim TK, Shin JH, Lee JK, et al. NADPH oxidase mediates depressive behavior induced by chronic stress in mice. J Neurosci. 2012;32(28):9690-9.
67. Arakawa H, Arakawa K, Blanchard DC, Blanchard RJ. Scent marking behavior in male C57BL/6J mice: sexual and developmental determination. Behav Brain Res. 2007;182(1):73-9.
68. Borelli KG, Blanchard DC, Javier LK, Defensor EB, Brandao ML, Blanchard RJ. Neural correlates of scent marking behavior in C57BL/6J mice: detection and recognition of a social stimulus. Neuroscience. 2009;162(4):914-23.
69. Arakawa H, Arakawa K, Blanchard DC, Blanchard RJ. A new test paradigm for social recognition evidenced by urinary scent marking behavior in C57BL/6J mice. Behav Brain Res. 2008;190(1):97-104.
70. McQuaid RJ, Audet MC, Anisman H. Environmental enrichment in male CD-1 mice promotes aggressive behaviors and elevated corticosterone and brain norepinephrine activity in response to a mild stressor. Stress. 2012;15(3):354-60.
71. Khalil V, Faress I, Mermet-Joret N, Kerwin P, Yonehara K, Nabavi S. Subcortico-amygdala pathway processes innate and learned threats. Elife. 2023;12.

Acknowledgments:

We thank Y. Tao and X. Hu for sharing *Nestin-cre* and *Emx1-cre* mice. We thank Y. Zhu for sharing psychological knowledge to facilitate our understanding of data. We thank Y. Niu for KEGG map drawing. We thank Westlake University Laboratory Animal Resource Centre for guiding behaviour assays. We thank the Microscopy Core Facility of Westlake University for imaging guidance. We thank the Mass Spectrometry & Metabolomics Core Facility (MSMCF) of Westlake University for mass data collection. We thank the Flow Cytometry Core Facility (FCCF) for cell sorting assistance.

Funding:

J.-M.J. acknowledges the support from Westlake Laboratory of Life Sciences and Biomedicine (project No. 202309002), Westlake University startup funding, the Westlake Education Foundation, Zhejiang, Key R&D Program of Zhejiang (2024SSYS0031), and the National Natural Science Foundation of China (project No. 32170961).

Author contributions:

J.-M.J. conceived the project, designed the experiments, and supervised this study. J.R. did primary experiments, obtained and organized majority original data, and wrote the manuscript draft. X.Q participated in behavioural assay design and operations, siRNA cisternal magna injection, gut health inspection assay, BBB integrity inspection, cluster analysis of similarity index, and wrote Mann-Whitney U test R code. H.X. participated in the looming assay and VR_{eagle} assay, as well as in blood pressure measurement and long-term whisker stimulation. Y.Z wrote the main MATLAB code. D.Z provided primer pairs of Grin1 and critical suggestions. W.W contributed to the writing of MATLAB code with Y.Z. B.Z. participated in the genotyping of mice and cell sorting. D.L. helped the mouse brain section.

Competing interests:

The authors declare that they have no competing interests.

Data and materials availability:

Necessary data needed to evaluate the conclusions in the paper are present in the paper and/or the Supplementary Materials. More information please contact the corresponding author.

Figure 1

Ruan et al.,

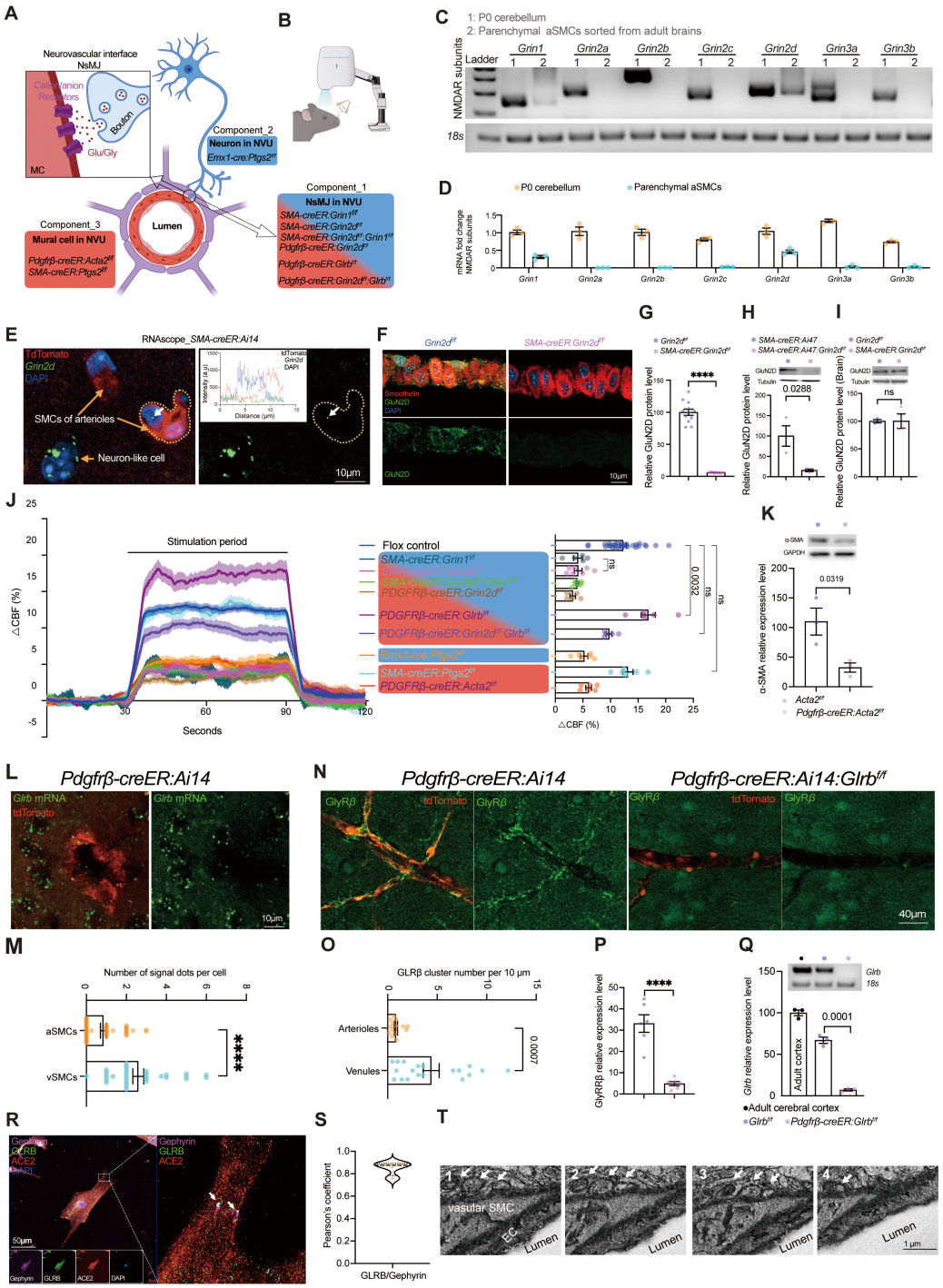

Fig. 1. Bidirectional NVC genetic models. (A) The schematic diagram of three components in NVU targeted by genetic manipulations. **(B)** The schematic diagram of LSCI recording while whisker stimulation. **(C)** mRNA expression levels of all subunits of NMDARs in primary aSMCs. **(D)** The quantification for Figure. 1C. **(E)** RNAscope detection of *Grin2d* transcripts in brain slices of *SMA-creER:Ai14* mice. The white arrow pointed to *Grin2d* mRNA, plotted in the inserted histogram. **(F)** The immunofluorescence staining of GluN2D in the arterioles of *Grin2d*$^{f/f}$ and *SMA-creER:Grin2d*$^{f/f}$ mice. **(G)** The quantification for Figure. 1F. **(H)** The expression of GluN2D in the sorted aSMCs from *SMA-creER:Ai47* and *SMA-creER:Ai47:Grin2d*$^{f/f}$ mice. **(I)** The expression of GluN2D in the cerebral cortex of *Grin2d*$^{f/f}$ and *SMA-creER:Grin2d*$^{f/f}$ mice. **(J)** CBF changes in barrel cortex upon whisker stimulation. The mean of CBF changes from individual mice plotted in the right panel. **(K)** The expression of α-SMA in the cerebral cortex of *Acta2*$^{f/f}$ and *Pdgfrβ-creER:Acta2*$^{f/f}$ mice. **(L)** RNAscope detection of *Glrb* transcripts in brain slices of *Pdgfrβ-creER:Ai14* mice. **(M)** The quantification of mRNA signal dots in aSMCs and vSMCs for Figure. 1M. **(N)** The expression of GlyR*β* in brain slices of *Pdgfrβ-creER:Ai14* and *Pdgfrβ-creER:Glrb*$^{f/f}$*:Ai14* mice. **(O)** The statistical data of GlyR*β* clusters in aSMCs and vSMCs of *Pdgfrβ-creER:Ai14* mice in Figure. 1N. **(P)** The quantification of GlyRβ immunosignal intensity for Figure. 1N. **(Q)** Semi-quantitative analysis of *Glrb* mRNA by RT-PCR for the sorted PDGFRβ^{+} cells in the cerebral cortex of *Glrb*$^{f/f}$ and *Pdgfrβ-creER:Glrb*$^{f/f}$ mice. **(R)** Co-immunostaining of GlyR*β* and Gephyrin in vSMC cell line. The white arrow marked their colocalizations. **(S)** The statistical co-localization analysis for Figure. 1R. **(T)** Serial SEM sections of the ascending venule in mouse cerebral cortex. The white arrows point to presynaptic boutons of NsMJ in venules. Data are presents as mean ± SEM.

Figure 2

Ruan et al.,

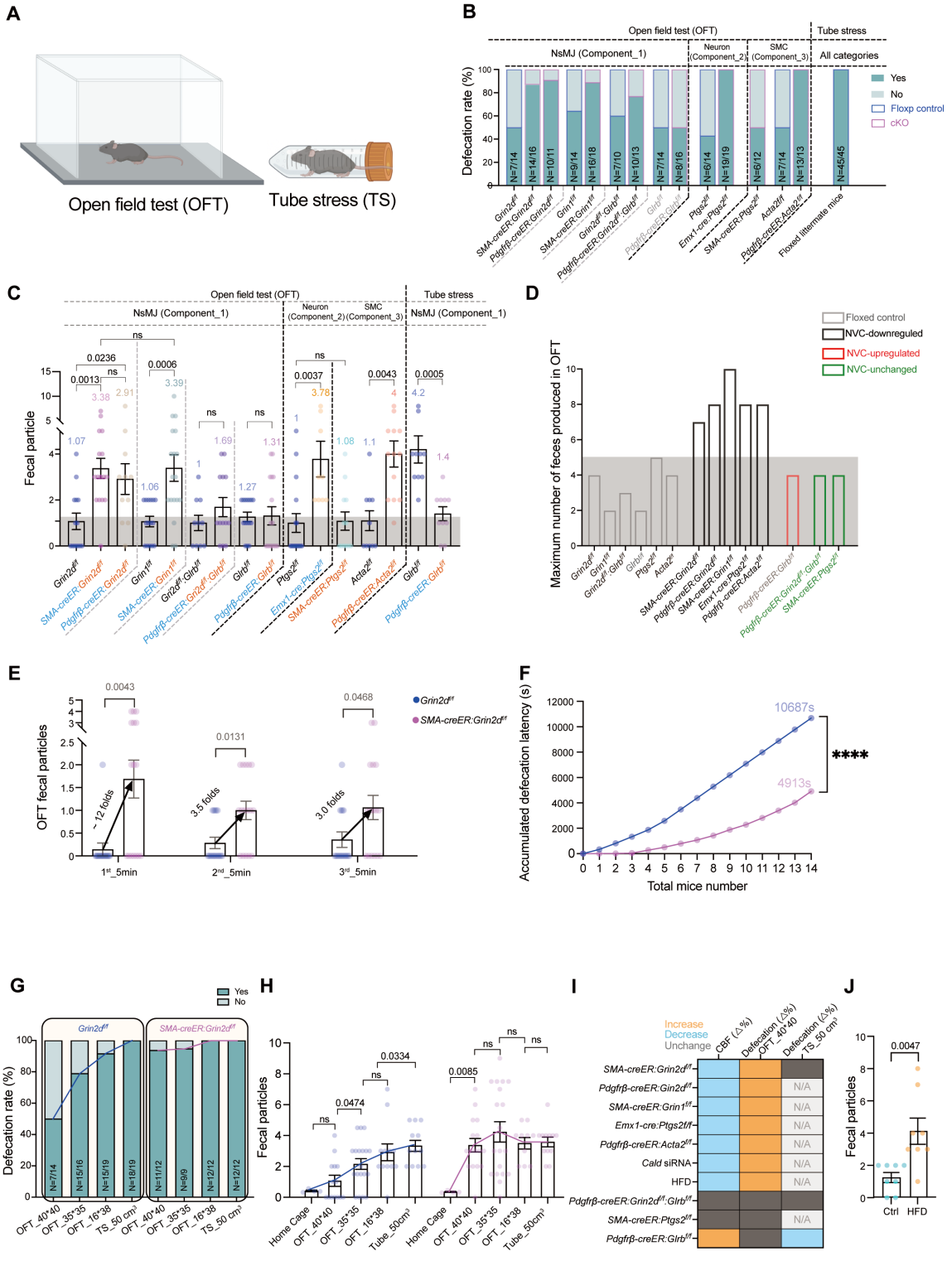

Fig. 2. NVC is required to actively modulate the capacity of flexible emotion regulation. (A) The schematic diagram of the OFT and Tube stress. **(B)** The defecation rates of each mouse line subjected to the assay of OFT_40*40 and that of all summed six floxed control lines subjected to tube stress. **(C)** The total number of fecal particles produced by each line within a 15-minute period of OFT_40*40 and that produced by the *Glrb* gene-modified lines within the same period of tube stress. **(D)** The maximum feces number produced by each line subjected to the OFT_40*40 assay. Raw data generating B-D panels shared the same bunch of mice. Mouse numbers (N) used for each line were listed in Figure. 2B. **(E)** The feces production within every 5 minutes during the 15-minute OFT_40*40 assay, N = 14 mice for the blue group and 16 mice for magenta. **(F)** The cumulative defecation latency summarized from fourteen mice for each genotype subjected to the OFT_40*40 assay. **(G)** The defecation rates for the OFTs of 40*40 cm^2, 35*35 cm^2, 16*38 cm^2, and the 50 cm^3 tube assay. **(H)** The total number of fecal particles produced in Figure. 2G. The raw data generating C (*Grin2d*$^{f/f}$ and *SMA-creER:Grin2d*$^{f/f}$), G and H shared the same bunch of mice, and the total mouse number (N) used is listed in Figure. 2H. **(I)** The negative correlative relationship between NVC changes and defecation activity recorded in the assays of OFT_40*40 and tube stress. **(J)** The fecal production in OFT_40*40 of normal mice with or without prior HFD challenge. Data are presents as mean ± SEM.

Figure 3

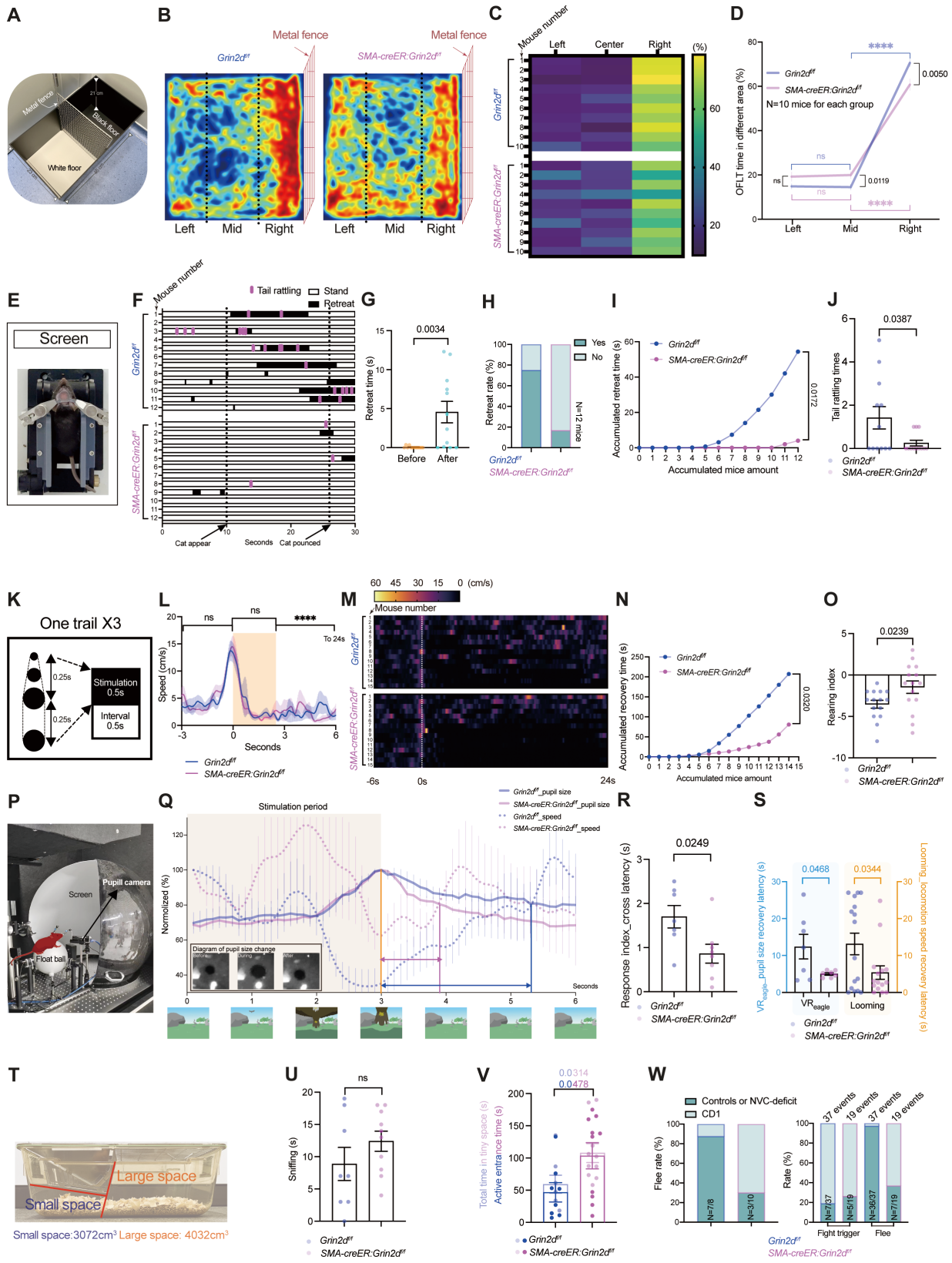
A
Metal fence
Black floor
White floor
B
Metal fence
Metal fence
Grin2df/f
SMA-creER:Grin2df/f
Left
Mid
Right
C
Mouse number
Left
Center
Right
(%)
D
OFLT time in different area (%)
N=10 mice for each group
0.0050
0.0119
ns
****
E
Screen
F
Mouse number
Tail rattling
Stand
Retreat
Cat appear
Seconds
Cat pounced
G
0.0034
Retreat time (s)
Before
After
H
Retreat rate (%)
Yes
No
N=12 mice
I
Accumulated retreat time (s)
Accumulated mice amount
0.0172
J
0.0387
Tail rattling times
K
One trail X3
0.25s
Stimulation 0.5s
Interval 0.5s
L
Speed (cm/s)
Seconds
To 24s
M
(cm/s)
Mouse number
-6s
0s
24s
N
Accumulated recovery time (s)
Accumulated mice amount
0.0220
O
0.0239
Rearing index
P
Screen
Pupil camera
Float ball
Q
Stimulation period
Normolized (%)
Diagram of pupil size change
Seconds
R
0.0249
Response index_cross latency (s)
S
0.0468
0.0344
VReagle_pupil size recovery latency (s)
Looming_locomotion speed recovery latency (s)
VReagle
Looming
T
Large space
Small space
Small space:3072cm³ Large space: 4032cm³
U
ns
Sniffing (s)
V
0.0314
0.0478
Total time in tiny space (s)
Active entrance time (s)
W
Controls or NVC-deficit
CD1
Flee rate (%)
N=7/8
N=3/10
Rate (%)
37 events
19 events
37 events
19 events
N=7/37
N=5/19
N=36/37
N=7/19
Fight trigger
Flee

Fig. 3. NVC is required to actively modulate the innate fear response. (A) The schematic diagram of the OFLT box setting. **(B)** The schematic diagram of the trajectory heat map of *Grin2d*$^{f/f}$ and *SMA-creER:Grin2d*$^{f/f}$ mice in the OFLT. **(C)**The heat map of mice stay rate in the left, middle, and right areas of the OFLT box. **(D)** The statistical data of Figure 2C. **(E)** The schematic diagram of Cat_{video} assay. **(F)** The locomotion pattern of *Grin2d*$^{f/f}$ and *SMA-creER:Grin2d*$^{f/f}$ mice during the Cat_{video} assay. **(G)** The retreat time of *Grin2d*$^{f/f}$ mice before and after cat appearance during the Cat_{video} assay. **(H)** The retreat rate of *Grin2d*$^{f/f}$ and *SMA-creER:Grin2d*$^{f/f}$ in the Cat_{video} assay after cat appearance. **(I)** The retreat time accumulation curve of *Grin2d*$^{f/f}$ and *SMA-creER:Grin2d*$^{f/f}$ mice in the Cat_{video} assay after cat appearance. **(J)** The tail rattling times of *Grin2d*$^{f/f}$ and *SMA-creER:Grin2d*$^{f/f}$ mice in the Cat_{video} assay after cat appearance. (K) The schematic diagram of looming assay. **(L)** The diagram of locomotion speed of *Grin2d*$^{f/f}$ and *SMA-creER:Grin2d*$^{f/f}$ mice from -3s to 6s in the looming assay. **(M)** The locomotion speed heat map of *Grin2d*$^{f/f}$ and *SMA-creER:Grin2d*$^{f/f}$ mice from -6s to 24s in the looming assay. **(N)** The freezing status recovery latency accumulation curve of *Grin2d*$^{f/f}$ and *SMA-creER:Grin2d*$^{f/f}$ mice in the looming assay. **(O)** The rearing index of *Grin2d*$^{f/f}$ and *SMA-creER:Grin2d*$^{f/f}$ mice in the looming assay. It is calculated by the rearing times after stimulation minus that before the stimulation. **(P)** The exterior of the VR stimulation system. **(Q)** The normalized pupil size and locomotion speed of *Grin2d*$^{f/f}$ and *SMA-creER:Grin2d*$^{f/f}$ mice in the VR_{eagle} assay. **(R)** The statistical data of response index from Figure. 3Q. **(S)** The statistical data of pupil size recovery latency and looming locomotion recovery latency from Figure. 3M and Figure. 3Q. **(T)** The schematic diagram of CD1 social assay box setting. **(U)** The sniffing times during the CD1 social assay. **(V)** The total time of *Grin2d*$^{f/f}$ and *SMA-creER:Grin2d*$^{f/f}$ mice together with aggressive CD1 mouse in the small space (light color), and the time of *Grin2d*$^{f/f}$ and *SMA-creER:Grin2d*$^{f/f}$ mice in the small space when CD1 mice already stayed in the small space (deep color). **(W)** The total flee rate of *Grin2d*$^{f/f}$ and *SMA-creER:Grin2d*$^{f/f}$ mice (counted as per mouse) after fight with aggressive CD1 mouse (left), and the normalized flee rate of *Grin2d*$^{f/f}$ and *SMA-creER:Grin2d*$^{f/f}$ mice (counted as per fight event) after fight with aggressive CD1 mouse (right). Data are presents as mean ± SEM.

Figure 4

Ruan et al.,

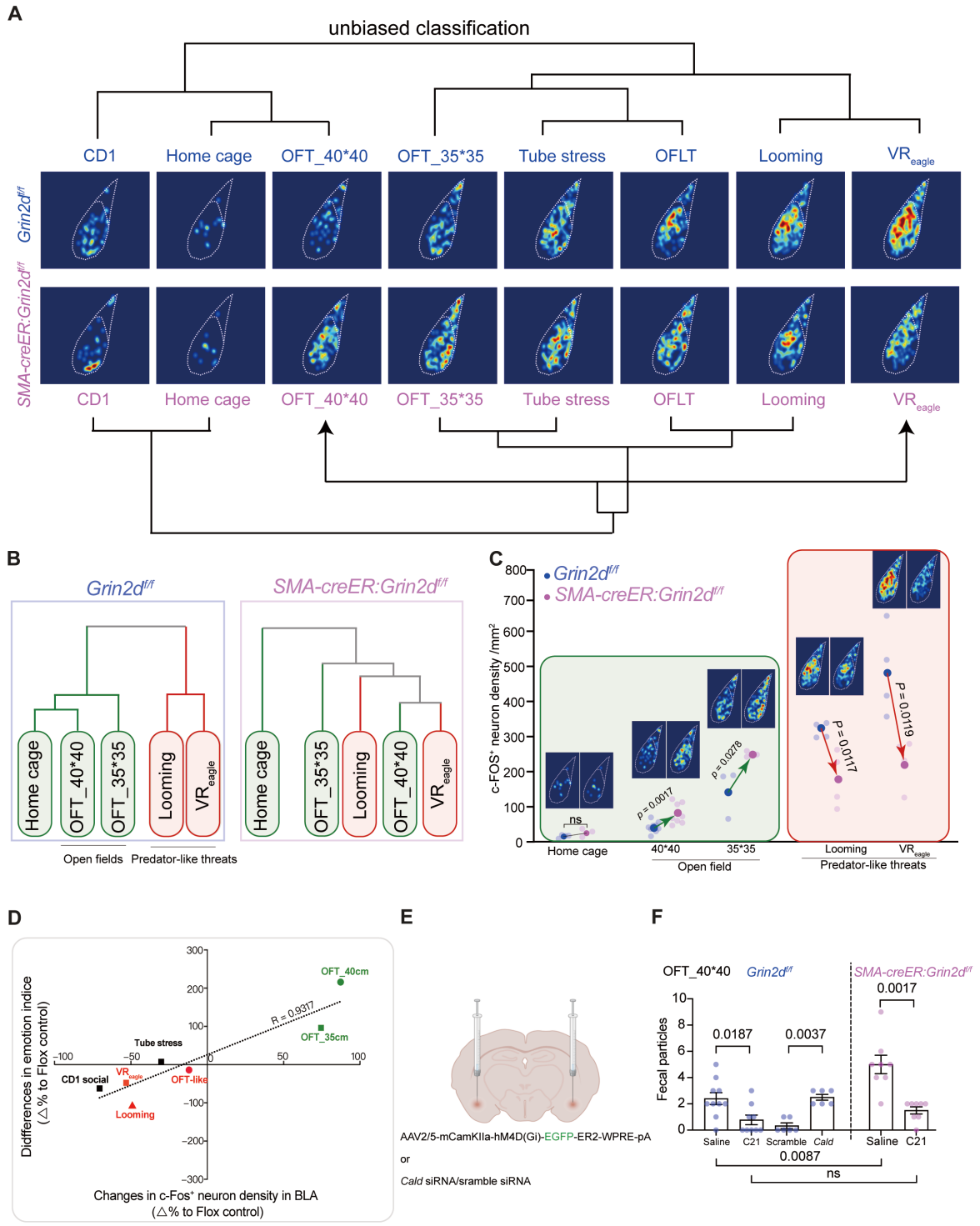

Fig. 4. NVC differentially regulates BLA neural activation. (A) Similarity index-based unbiased classification of c-Fos^{+} neuron distribution pattern in BLA of the two genotypic lines across eight different contexts. **(B)** A similar classification as in a except for excluding tube stress, OFLT, and CD1 contexts. **(C)** Quantification of the density of c-Fos $^{+}$ neurons in BLA under five contexts. **(D)** Correlation between the level of BLA activation and the level of emotion indices. Hyper-response (higher emotion indices) mirrored with higher c-Fos^{+} neuron density in BLA (green marks); Hypo-response (lower emotion indices) mirrored with lower c-Fos^{+} neuron density (red marks). **(E)** The schematic diagram of virus/siRNA injection to the BLA. **(F)** The fecal particles produced in OFT_40*40 by *Grin2d*$^{f/f}$ and *SMA-creER:Grin2d*$^{f/f}$ mice, respectively, after local manipulations in BLA by overexpression of hM4D (Gi) or knockdown caldesmon. Data are presents as mean ± SEM.

Figure 5

Ruan et al.,

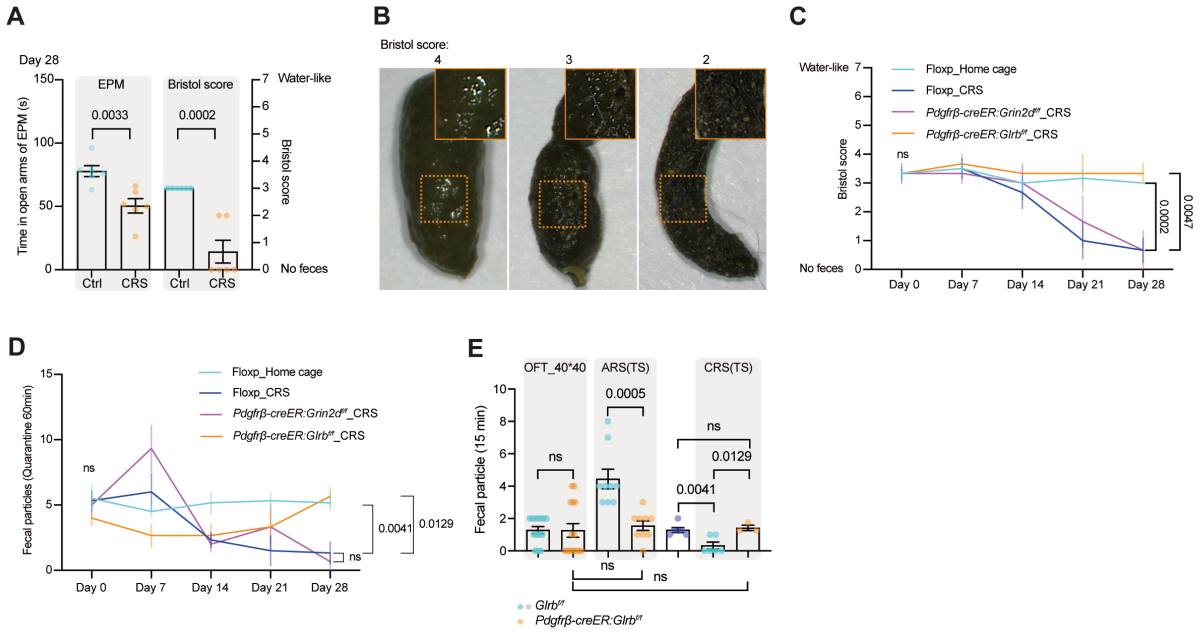

Fig. 5. The NVC-upregulation model showed emotional resistance to chronic restraint stress (CRS). (A) The total time spent in open arms of EPM before/after the CRS. **(B)** Representative images of stools scoring at 4, 3, and 2 according to Bristol assessment. **(C and D)**, Progressive changes in Bristol scores and fecal particle number produced within a period of 60 minutes. The evaluation was performed every week for consecutive 4 weeks of CRS. **(E)** Profiling of differential defecation behavioral responses of the two genotypic lines across three contexts of OFT_40*40, acute restriction tube stress (ARS), CRS. The raw data of OFT_40*40 and ARS from Figure 2C. Data are presents as mean ± SEM.

Science
AAAS

Supplementary Materials for

Neurovascular coupling actively regulates context-dependent emotional adjustment

Authors: Jiayu Ruan, Xinghua Quan, Huiqi Xie, Yiyi Zhang, Dongdong Zhang, Wentao Wang, Bingrui Zhao, Danping Lu, Jie-Min Jia*

*Corresponding author. Email: Jie-Min Jia (jiajiemin@westlake.edu.cn)

The PDF file includes:

Materials and Methods
Figs. S1 to S15
Tables S1 to S3

Other Supplementary Materials for this manuscript include the following:

Movies S1
Movies S2

Materials and Methods

Animal and animal care

All mouse procedures complied with the Institutional Animal Care and Use Committee (IACUC) guidelines of the School of Life Sciences, Westlake University. All mice were housed in the Westlake University Laboratory Animal Resource Centre with standard animal facilities, which provided a 12-hour light/dark cycle at 25°C. No more than six mice were fed each cage, and standard chow/water were provided to the mice *ad libitum*. All the genetic information of mice is in Table S1.

Cell culture

SMA-creER:Ai47 P0 mice were anesthetized with ice. Surgical tweezers were used to quickly extract the cortex and then transfer it into the 0.25% Trypsin (Thermo Scientific, Cat# 25200072, USA) for 15 minutes at 37°C. Next, FBS (Gibico, Cat# 10099, USA) was added to block digestion. Then, cells were filted by a 40 μm filter (Falcon, Cat# 352340, CHN). Finally, cells were centrifuged 1,600*g at 4°C for 5 minutes and resuspended by SMCM (ScienCell, Cat# 1101, USA) in T25 flasks (Corning, Cat# 430639, USA). When cells reached approximately 80% full of the bottom surface of T25 flasks, tamoxifen (MCE, Cat# HY-13757A, USA) was administrated to cells. Tamoxifen was dissolved in DMSO (Solarbio, Cat# D8371, CHN), and the final concentration of tamoxifen was 5 μM. After a four-day culture, EGFP in cells were expressed. Cells were sorted by MA-900 (Sony, FCCF-MBR, JPN) to obtain $EGFP^+$ cells. Sorted cells were cultured in SMCM for further assay. The purity of cells sorted by the same method was verified in a paper published by our laboratory *(56)*. For data in Figure. 1Q, samples were directly sorted from *Pdgfrβ*$^+$cells in brain lysis. Then, *Pdgfrβ*$^+$cells were quickly resuspended by Trizol (Sangon Biotec, Cat# B511311-0100, CHN) for RNA extraction.

RT-PCR

For cultured cells, after obtaining pure sorted $EGFP^+$ cells from the cortex, cells were cultured in 6 cm dishes (Corning, Cat# 430166, USA) with SMCM. After cells reached around 90% density, Trizol was used for the RNA extraction. For brain tissue, after mice were anesthetized with ice, the cortex or cerebellum of the mice was directly taken out, and TRIzol was used for RNA extraction. After extraction, all RNA samples were reverse transcribed to cDNA (50ng/μl) using HiScript III 1st Strand cDNA Synthesis Kit (Vazyme, Cat# R312-02, CHN). For the Real-Time Polymerase Chain Reaction (RT-PCR), each reaction contained 10 μl of Green Taq Mix (Vazyme, Cat# P131-AA, CHN), 2 μl of cDNA, 2 μl of primer pairs (10μM), and 6 μl of RNAase-free water. Agarose gel electrophoresis used 2% agarose gel (BIOWESTE, Cat# 111860, ESP) and ran at 220V for 30min. RT-PCR gel images were obtained from a Tanon imager (Tanon, 1600 Geil imager, CHN). A list of primer pairs is in Table S2.

RNA scope in situ hybridisation

Horizontal sections (15 μm) of tamoxifen administrated *SMA-creER:Ai14* (for *Grin2d*), *Pdgfrβ-creER:Ai14* (for *Glrb*) and C57 wild-type (for *Grin2d and Grin1* probe inspection) mice brains were obtained by CM1950 (Lecia, Histo-CM1950, DEU). All RNA scope *in situ* hybridisation productions were obtained from ACDbio, including RNAscope Multiplex Fluorescent Reagent Kit v2 (ACDbio, Cat# 323100, USA), *Grin2d* probe (ACDbio, Cat# 425951-C3, USA), *Grin1* probe (ACDbio, Cat# 431611, USA), and *Glrb* probe (ACDbio, Cat# 1225261-

C1, USA). All operations were carried out following the reagent instructions of ACDbio company and published papers *(34, 57)*.

Tamoxifen administration for mice

Tamoxifen was dissolved in corn oil (Aladdin, Cat# C116023-500ml, CHN) and orally administered to mice (10mg/ml, 200ul per mouse per day). For conditional knockout *Acta2*, tamoxifen was given from P21 to P24. Otherwise, tamoxifen was orally administered to mice from P60 to P63.

Immunofluorescence staining

For Immunofluorescence (IF) staining, after anesthesia with 1% pentobarbital sodium, the mice were perfused with 1X PBS (5 min) and 4% PFA in 1X PBS (5min) through the left ventricle to empty blood and fix tissue. Afterwards, tissue was extracted and fixed by 4% PFA in 1X PBS for 6 hours at 4 ℃. For samples like the brain and peripheral organs, samples were sliced into 50 μm (Leica, Histo-VT1200S, DEU). Then, treated samples by 1% Triton X-100 (Diamond, Cat# A110694-0500, CHN) and 0.25% NDS (Jackson Resources, Cat# 017-000-121, USA) in 1X PBS for 60 minutes at room temperature. After that, samples were rewashed three times by 1X PBS.

In the staining process, the primary antibody diluted with 0.1% Triton X-100 in 1X PBS was used to incubate samples overnight at 4 ℃. After the incubation, samples were washed with 1X PBS 10min (3 replicates). The corresponding secondary fluorescence-conjugated antibody diluted with 0.1% Triton X-100 in 1X PBS was used to incubate samples for 120 minutes at room temperature. After the incubation, samples were washed with 1X PBS 10min (3 replicates). After that, 1000X diluted Hoechst (AbMole, Cat# M5112, CHN) was used for nucleus staining. Finally, samples were covered by a glass slice with the mounting medium (SouthernBiotech, 0100-01, USA). Zeiss LSM800 (Zeiss, LSM800, DEU) microscopy was used for photography. A list of antibodies is in Table S3.

Western-bolt

For tissue sample collection, samples were ground with RIPA (Thermo Scientific, Cat# 89901, USA) in the tube on ice for 30min. For cells, after they reached around 90% density, the RIPA was used for protein extraction on ice for 30 minutes. Protease Inhibitor Cocktail (CWBIO, Cat# CW22008, CHN) was added into RIPA to prevent protein enzymolysis. After that, samples were centrifuged at 12,000*g at 4℃ for 5min, and the supernatant was collected. Concentrations of proteins were measured by Micro BCA Protein Assay kit (CWBIO, Cat# CW2011S, CHN), and all samples were boiled with SDS-PAGE loading buffer (CWBIO, Cat# CW0027S, CHN) for 10min at 100℃. 8% SDS-polyacrylamide electrophoresis gels were used for gel running. After 90 minutes, gels running at 120V (80V for the first 30min), gels were transferred to 0.45 μm PVDF membranes (Millipore, Cat# IPVH00010, USA) at 400mA for 120min. After transfer, PVDF membranes were blocked by 5% non-fat milk in 1X TBST buffer for 60 minutes at room temperature with a mild horizontal shake.

After the block, the primary antibody diluted with 5% non-fat milk in 1X TBST buffer was used to incubate the membrane overnight at 4℃ with a mild horizontal shake. After the incubation, the membrane was washed by 1X TBST 10min (3 replicates). The corresponding secondary HRP-conjugated antibody diluted with 5% non-fat milk in 1X TBST buffer was used to incubate the membrane 45min at room temperature with a mild horizontal shake. After the incubation, the membrane was washed by 1X TBST 10min (3 replicates). ECL kits (Abbkine, Cat# BMU102-CN,

CHN) and gel image system (GE, GEL Imaging System AI680RGB v.2.0, USA) were used for exposure photography. Some primary antibodies are HRP-conjugated, so the use of secondary antibodies is not required. A list of antibodies is in Table S3.

Whisker stimulation

Mice were anesthesia with 1% pentobarbital sodium and open the scalp, then mice stable fixated on the holder. The electro-motor-driven brush stimulated the whisker longitudinally for 1 minute at a frequency of 12Hz. The principle of laser speckle contrast imaging has been described in the previous paper (21), and the operation referred to in the published paper *(34, 58, 59)*. Laser Speckle Image System (RWD, RFSLI ZW/RFSLI III, CHN) was used to monitor the CBF change in the ROI of the opposite barrel cortex of mice. The recording parameters were 512*512 resolution, 10FPS, and 2-minute recording. For long-term stimulation impact assay, data recording was performed on the first and last days of long-term stimulation. The mouse scalp was sutured after the first recording. Subsequent stimulations did not record data until the last stimulation. Code for CBF changes during the stimulation can be found at https://github.com/JialabEleven/.

Serial block-face scanning electron microscopy image

The specimen was obtained in the same batch as the previously published paper from our laboratory *(34)*. The details can be seen in the "SBF-SEM imaging" section of the methods in that paper. In brief, the ascending venule was identified using X-ray microscopy (Zeiss, XRM, Xradia 520 Versa, DEU) at ×4 and 80 kV magnification. The specimen adhered to an aluminum metal pin using conductive epoxy (Chemtronics, CW2400, USA). Then, it was further precisely trimmed into a block of 600*600*700 μm^3 using a glass knife and a right-angled diamond knife (DiATOME, Trim 90, CHE) after coating with gold-palladium (Leica, EM ACE200, DEU) and a final trim using a 3View ultramicrotome (Gatan, USA). Image acquisition was performed using a BSE detector on a Carl Zeiss Gemini 300 scanning electron microscope at 2 kV voltage and approximately $1.8*10^{-3}$ mBar in high-vacuum mode with focus charge compensation. The specimens were sectioned at a 50–75 nm thickness and a cutting speed of 0.1 mm/s.

siRNA cisternal magna/BLA local injection and whisker stimulation

All cisterna magna injection referred to *Cannula Implantation into the Cisterna Magna of Rodents* (https://doi.org/10.3791/57378) and paper published by our laboratory *(34)*. siRNA (final concentration 1nM) was mixed with FITC (10mg/ml, Sigma, FD40S-1G, USA) for injection. The scalp was opened 10 minutes after the injection, and the microscope detected the FITC signal (Zeiss, Axio Zoom v16, DEU). Only successfully injected mice remain. Whisker stimulation and OFT was performed 48 hours after siRNA injection. As for BLA local siRNA injection, 150nl of siRNA (final concentration 1nM) was injected in two sides of BLA (AP:-1.6mm; ML:+/-3.45mm; DV:-4.1mm), and OFT was performed 48 hours after siRNA injection. Sequence of siRNA can be found in the Table S2.

Immunoprecipitation assay

$tdTomato^+$ sorted aSMCs from P0 *SMA-creER:Ai14* mice were used for lentivirus infection and further immunoprecipitation (IP) assay. Sorted cells were cultured in 6 cm dishes with SMCM. After cells reach around 90% density, add lentivirus (Lenti-EF1-EGFP-CMV-grin2d-3XFlag-WPRE, virus titer: $2.6*10^9$) into the culture and keep for one week to over-express GluN2D. MA-900 sorted out EGFP and tdTomato double-positive cells, which were lentivirus-infected aSMCs.

These cells were then cultured in 10 cm dishes. After cells reached around 90% density, cells were collected by RIPA reagent. The Protein G Magnetic beads kit (Epizyme, Cat# YJ002, CHN) was used for the immunoprecipitation assay. GluN2D and IgG control antibodies were mixed with Protein G Magnetic beads to pull down GluN2D and its related protein. Pull-down products were verified by western-bolt and analyzed through mass spectrometry. A list of antibodies is in Table S3. Code for data anyalsis can be found at https://github.com/JialabEleven/.

Home cage monitor assay

The blood pressure of mice was measured by Kent Noninvasive blood pressure measurement system for animals (Kent/Biopac, USA) before the mice were put into the home cage. Each home cage only contains four mice. In each cycle (three days), 60g of food, 340g of water (including bottle weight), and 100g of padding were provided. Weight of mice, food/water consumption, fecal particles, and urination amount (counted by increased padding weight) were measured. Three cycles of monitoring were performed for each home cage. After the assay, mice were fed alone in a clean new cage for 90 minutes and then used for brain extraction to detect c-Fos expression. The intestine system inspection was performed after three cycles of monitor.

BBB leakage inspection

2% evens blue (Merck, Cat#E2129, USA) in saline was used for orbital injection (4ul/g). After 45 minutes, the mouse was anesthetized, and the brain was extracted for appearance inspection for BBB leakage using a microscope (Zeiss, Axio Zoom v16, DEU). The brain was weighted and then homogenized using 1 ml of 50% trichloroacetic acid (Merck, Cat#190780, USA). Then, samples were centrifuged at 10,000*g at 4℃ for 20min, supernatants were collected, and absorbance detection at 620nm was performed.

Colorectal inspection

Representative images of colorectal tissue were taken by ENDOQ Colonscopy system. Scoring of the endoscopic images was performed by professional physician in a double-blind manner to ensure unbiased assessment.

Hematoxylin and eosin staining

For hematoxylin and eosin (HE) staining, after anaesthesia with 1% pentobarbital sodium, the mice were perfused with 1X PBS (5 min) and 4%PFA in 1X PBS (5min) through the left ventricle to empty blood and fix tissue. Afterwards, tissue was extracted and fixed by 4%PFA in 1X PBS for 6 hours at 4 ℃. After a paraffin block, tissues were sliced into 8 μm sections and examined following HE staining.

Open field test

The setup of open field test (OFT) referred to published papers *(60-63)*. Each mouse was placed in the central area of a 40*40 cm, 35*35 cm or 16*38cm box for the OFT. The camera recording was 15 minutes. For the chemogenetic manipulation assay, the C21 intraperitoneal injection was 45 minutes before the OFT. After the assay, mice were fed alone in a clean new cage for 90 minutes and then used for brain extraction to detect c-Fos expression.

Quarantine assay

The setup of quarantine assay is referred to as OFT. Each mouse was placed in the central area of an empty home cage box. The camera recording was 15 minutes. For the HFD challenge assay, the duration of the quarantine assay was 60 minutes, and defecation and urination were monitored. For the chemogenetic manipulation, mice were C21 intraperitoneal injected 45 minutes before the assay, and then each mouse was put into the box for 15 min.

Tube stress assay

A 50ml tube was used to restrain the mice *(39, 64, 65)* to perform acute restraint stress (ARS) and chronic restraint stress (CRS). The tube cover and wall will be drilled to ensure normal breathing. For ARS, the mice were restrained in the tube for 15 minutes, and then the fecal production was measured. For the ARS plus chemogenetic manipulation assay, the C21 intraperitoneal injection was 45 minutes before the tube stress assay. After the assay, mice were fed alone in a clean new cage for 90 minutes and then used for brain extraction to detect c-Fos expression. For CRS, the mice were restrained in the tube for 120 minutes/day, constant for 28 days, and fecal production and Bristol score was measured at the end of each seven days using 60min quarantine assays described above.

Open field-like test

The open field-like test (OFLT) setup referred to a published paper *(66)*.Each mouse was placed in the central area of the left part of OFLT box. One side of OFLT box has white bottom (mouse put into this side), and black bottom in another side.The camera recording was 15 minutes. For the analysis, the box was divided into three parts (left area, central area, and right area) to analyze the preference of mice for iron mesh wall (right area close to the iron mesh wall). After the assay, mice were fed alone in a clean new cage for 90 minutes and then used for brain extraction to detect c-Fos expression. Code for the generation of trajectory heatmap of mice can be found at https://github.com/JialabEleven/.

High fat diet challenge assay

Mice were given high-fat food (SYSE, Cat# PD6001, CHN) for four weeks. The weight of mice and food consumption were measured at the end of each week. The home cage fecal production was measured using the same method mentioned in the "Home cage monitor assay" part. OFT_40*40 assay and whisker stimulation assay were performed after four weeks of HFD challenge.

Cat Video stimulation assay

The assay was carried out in a 40*40 cm OFT box. The mouse head was fixed with a fixator and trained to fit the treadmill two weeks before the assay. On the day of the assay, the mice were anesthetized with isoflurane and fixed on the treadmill. After the mouse wakes up, play the video of cat hunting on the iPad in front of the mouse (Movie S1). Play the video three consecutive times, each time lasting 30 seconds. A camera directly above was used to record the assay.

Looming assay

The assay was carried out in a 35cm*35cm OFT box. The settings of the assay were based on the published paper *(52)*. Modifications include:

- mice will be put in the OFT box to adapt for 10 minutes before starting the assay;
- we only use a single camera at the top of the box to record;

• we stimulate the mice when they move and are not close to the box wall rather than continuously stimulating them.

Each mouse performs three stimulations. After the assay, mice were fed alone in a clean new cage for 90 minutes and then used for brain extraction to detect c-Fos expression.

VR assay

Assay set up referred published paper *(51)*. The mouse head was fixed with a fixator two weeks before the assay. The mice received daily adaptive training on the VR system one week before the assay. On the day of the assay, the mice were fixed on the VR system and given 5 minutes of adaptation. Unless stimulated, the screen in front of the mouse will always play the regular landscape video. The stimulation of the eagle lasts for three seconds. The eagle swoops down from far to near and plays the voice of the eagle at the beginning of the stimulation. There were five times of stimulation in total, and the criterion for the first stimulation was that the mice moved for the first time after 5 minutes of adaptation. The criteria for subsequent stimulation were that the last stimulation ended for at least 2 minutes, and the mice resumed movement. The assay ended 2 minutes after the last stimulation. The pupil changes and locomotion speed of mice were recorded. After the assay, mice were fed alone in a clean new cage for 90 minutes and then used for brain extraction to detect c-Fos expression. For VR_{eagle} encircle ABC (area between curves) calculations in figure. S13B, in brief, we first shift the row data of locomotion speed and pupil size into Z-score, and then we calculate the encircle area by curves of locomotion speed and pupil size from before stimulation to post-stimulation. The larger the encircling area, the more intense the response to the stimulus (because there is a negative correlation between pupil size and locomotion speed when the stimulation reaches its peak).

CD1 social assay

The setup of CD1 fear assay referred to published papers *(66-69)*. Aggressive CD1 mice never exposed to *Grin2d*$^{f/f}$ or *SMA-creER:Grin2d*$^{f/f}$ mice were used for the assay. Before the assay, simultaneously put a single *Grin2d*$^{f/f}$ or *SMA-creER:Grin2d*$^{f/f}$ mouse and a CD1 mouse into a cage. The cage contains new padding and a metal lid on the top. One side of the metal lid is used to place food and water bottles, so the height is lower than the other. After that, the camera was used to record all the behaviours of two mice for 10 minutes. After the assay, mice were separated again. *Grin2d*$^{f/f}$ or *SMA-creER:Grin2d*$^{f/f}$ mice were fed alone in a clean new cage for 90 minutes and then used for brain extraction to detect c-Fos expression.

Chemogenetical manipulation

AAV2/5-mCaMKIIa-hM4D(Gi)-EGFP-ER2-WPRE-pA (2.30E+12VG/ml) or AAV2/5-mCaMKIIa-EGFP-ER2-WPRE-pA (2.30E+12VG/ml), were used for Chemogenetical manipulation. Two weeks before the assay, bilateral amygdala injection (150nl on each side, AP:-1.6mm; ML:+/-3.45mm; DV:-4.1mm) was administered *(70)*.

Statistical analysis software and code

All the image processing and analysis of fluorescence intensity used Zeiss Zen Lite (v3.4) and ImageJ (v1.53u). All whisker stimulation original data were measured by LSCI-self software (v5.0). All the original behavioural data for OFT/OFLT were recorded using Noldus. Data recording and analysis of Looming and VR_{eagle} assay was performed using self-compiled MATLAB codes provided by Bayonne company. All statistical data were processed by Numbers

(v12.2). Unless otherwise specified, t-tests were used for differential analysis on all data that conform to a normal distribution. Non-continuous data that does not conform to a normal distribution, such as fecal particles, signal dots in vessels, and rearing index were analyzed using the Mann-Whitney U test. All figures were made by Prism (v9.4.1) and Adobe Illustrator 2024 (v28.3). CBF peak mean value, heat maps, mass spectrometry data inclusion criteria, and similarity index (Based on the Structural Similarity Index, SSIM) were analyzed by self-compiled MATLAB codes. Besides, the KEGG pathways, c-Fos expression pattern classification, and Mann-Whitney U test were analyzed using self-compiled R code. All available code can be found at https://github.com/JialabEleven/.

Figure S1

Ruan et al.,

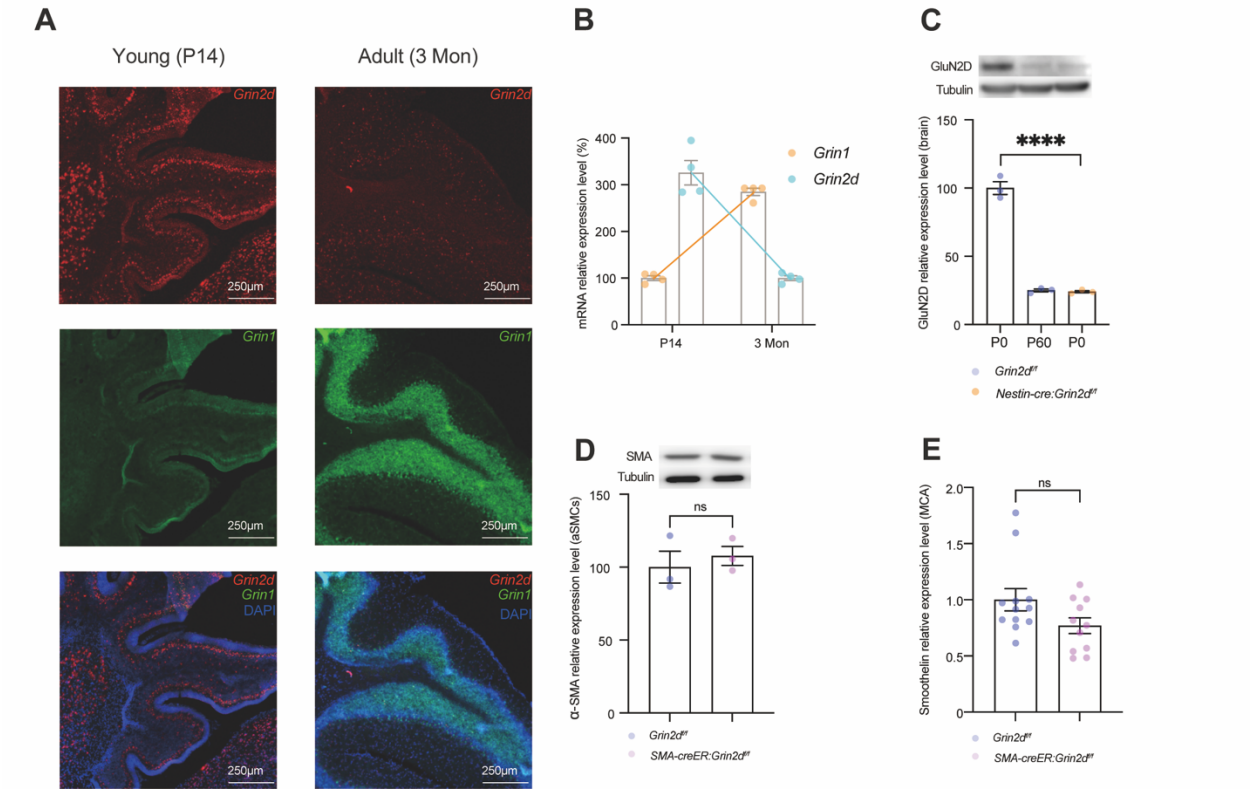

Fig. S1. Validation of RNAscope and *Grin2d*^{cko}. (A) RNAscope detection of *Grin1* and *Grin2d* transcripts in the cerebellum of brain slices from P14 and 3-month-old mice. **(B)** The quantification for figure. S1A. **(C)** The expression of GluN2D in cortex of P0 *Grin2d*$^{f/f}$, P60 *Grin2d*$^{f/f}$, and P0 *Nestin-cre:Grin2d*$^{f/f}$ mice. **(D)** The expression of α-SMA in cortex of *Grin2d*$^{f/ff}$ and *SMA-creER:Grin2d*$^{f/f}$ mice. **(E)** The expression of smoothelin in aSMCs of *Grin2d*$^{f/ff}$ and *SMA-creER:Grin2d*$^{f/f}$ mice. Data are presents as mean ± SEM.

Figure S2

Ruan et al.,

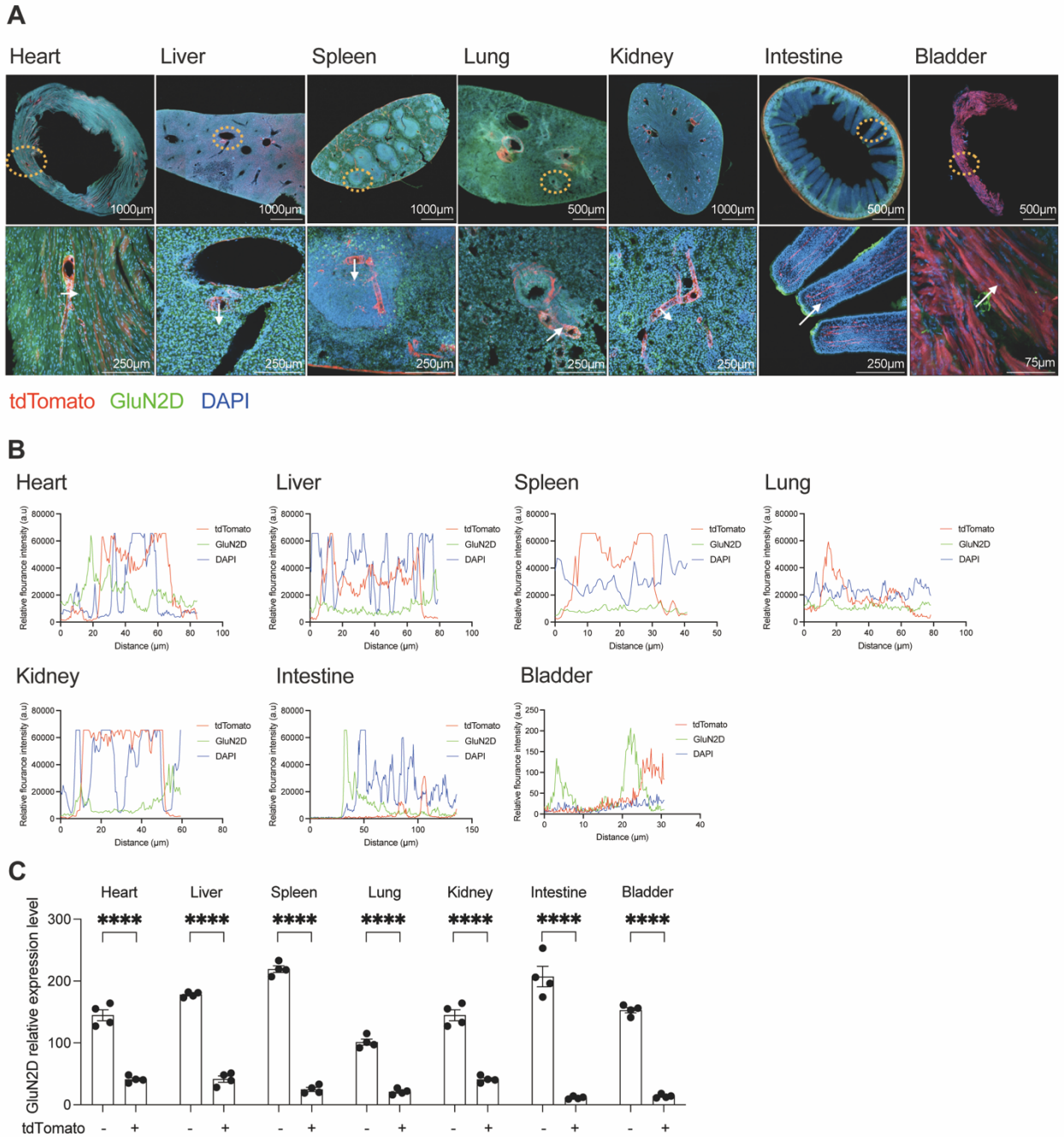

Fig. S2. Expression patterns of GluN2D in peripheral organs. (A) The protein expression of GluN2D in heart, liver, spleen, lung, kidney, small intestine, and bladder of *SMA-creER:Ai14* mice. The white arrow marked the ROI for profile analysis. **(B)** The line profiles of signal distribution of fig. S2A. **(C)** The quantification of GluN2D immunofluorescence density in the tdTomato^{-} ROIs and tdTomato^{+} ROIs. Data are presents as mean ± SEM.

Figure S3

Ruan et al.,

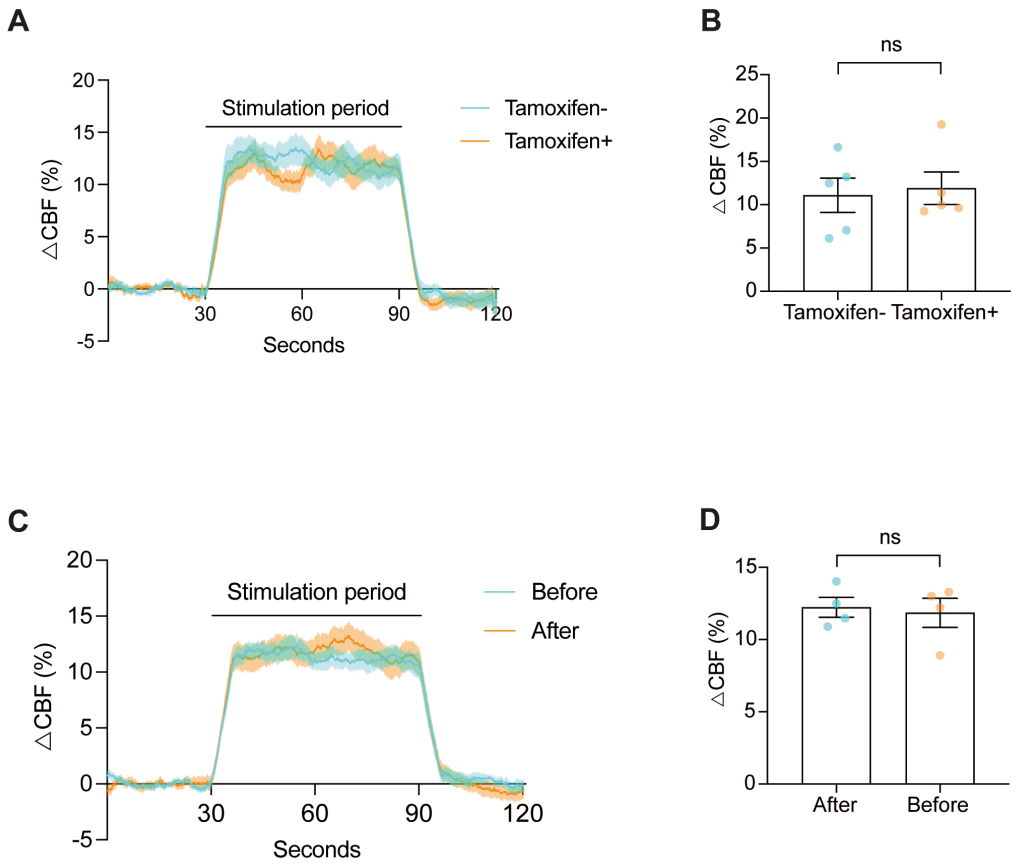

Fig. S3. The impact of tamoxifen and long-term-repeated whisker stimulation on the extend of functional hyperaemia during the whisker stimulation. (A) CBF changes of mice before/after the tamoxifen administration during the whisker stimulation. (B) The quantification for figure. S3A. **(C)** CBF changes of mice before/after the long-term-repeated whisker stimulation. **(D)** The quantification for figure. S3C. Data are presents as mean ± SEM.

Figure S4

Ruan et al.,

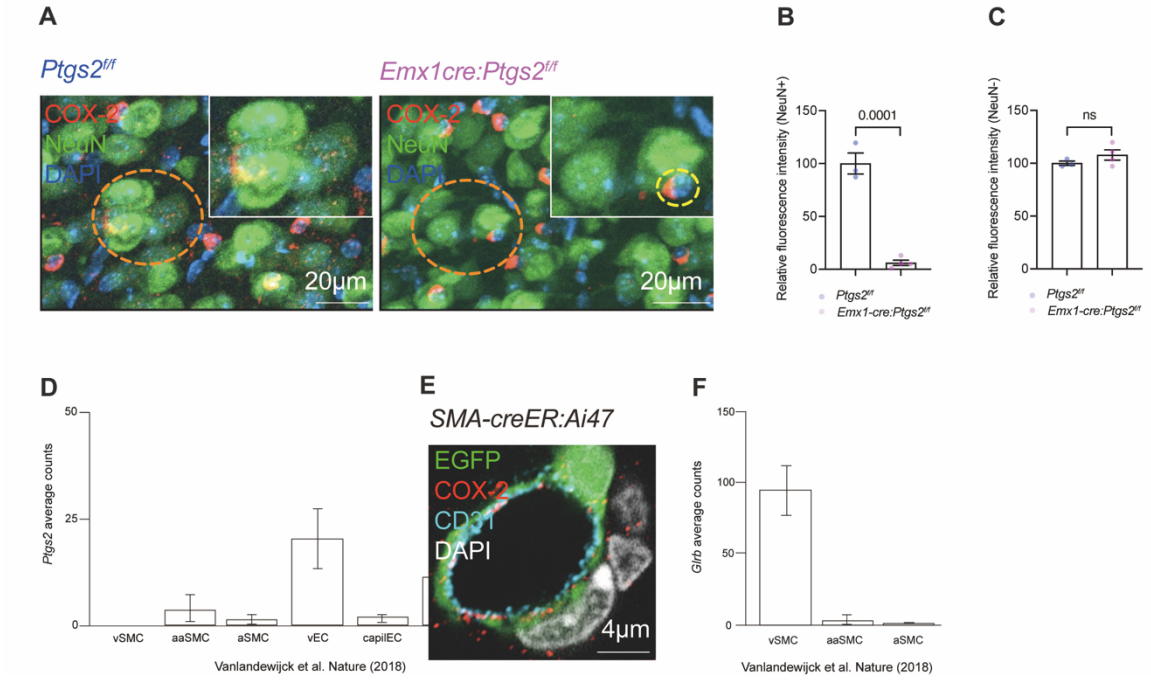

Fig. S4. The expression and validation of COX2 and *glrb*. (A) The immunofluorescence staining of COX2 in the brain slice of *Ptgs2*$^{f/f}$ and *Emx1-cre:Ptgs2*$^{f/f}$ mice. right up panel is the zoom-in orange circle encircled area. **(B)** The quantification of NeuN^{+} cells in fig. S4A. **(C)** The quantification of NeuN^{-} cells (shown in the yellow circle) in fig. S4A. **(D)** The mRNA expression level of *Ptgs2* from the data base. **(E)** The schematic diagram of COX2 expression pattern in cerebral blood vessels. **(F)** The mRNA expression level of *glrb* from the data base. Data are presents as mean ± SEM.

Figure S5

Ruan et al.,

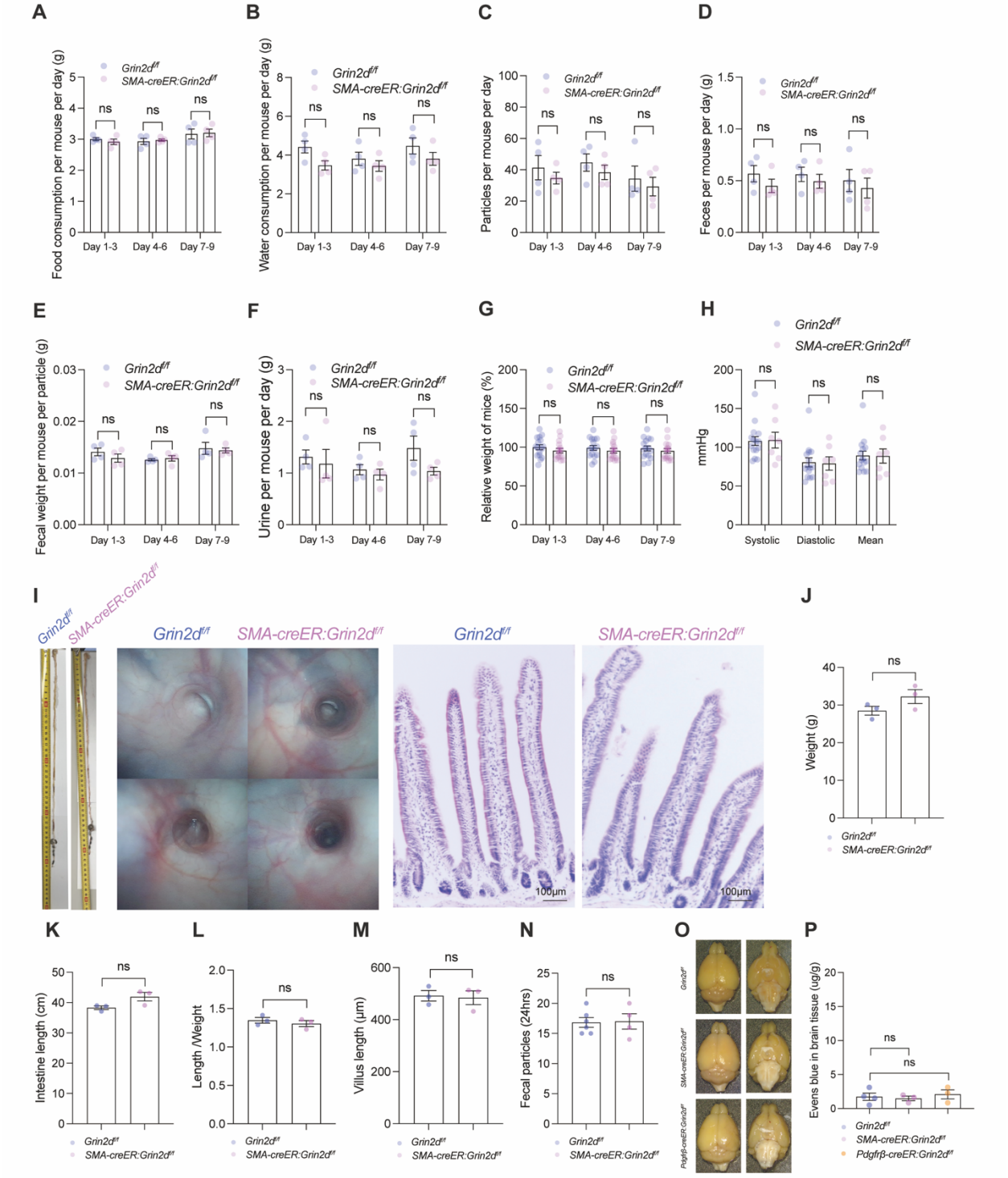

Fig. S5. Physical parameters inspection of *Grin2d*$^{f/ff}$ and *SMA-creER:Grin2d*$^{f/f}$ mice. (A) The food consumption of *Grin2d*$^{f/ff}$ and *SMA-creER:Grin2d*$^{f/f}$ mice. **(B)** The water consumption of *Grin2d*$^{f/ff}$ and *SMA-creER:Grin2d*$^{f/f}$ mice. **(C)** The fecal production of *Grin2d*$^{f/ff}$ and *SMA-creER:Grin2d*$^{f/f}$ mice per day. **(D)** The fecal weight of *Grin2d*$^{f/ff}$ and *SMA-creER:Grin2d*$^{f/f}$ mice per day. **(E)** The weight of each fecal particle of *Grin2d*$^{f/ff}$ and *SMA-creER:Grin2d*$^{f/f}$ mice. **(F)** The urine amount of *Grin2d*$^{f/ff}$ and *SMA-creER:Grin2d*$^{f/f}$ mice. **(G)** The weight change of *Grin2d*$^{f/ff}$ and *SMA-creER:Grin2d*$^{f/f}$ mice. **(H)** The blood pressure of *Grin2d*$^{f/ff}$ and *SMA-creER:Grin2d*$^{f/f}$ mice. **(I)** Left, the schematic diagram of gut system appearance inspection of *Grin2d*$^{f/ff}$ and *SMA-creER:Grin2d*$^{f/f}$ mice; mid, the schematic diagram of colorectal endoscopy inspection of *Grin2d*$^{f/ff}$ and *SMA-creER:Grin2d*$^{f/f}$ mice; right, the schematic diagram of small intestine hematoxylin-eosin staining of *Grin2d*$^{f/ff}$ and *SMA-creER:Grin2d*$^{f/f}$ mice. **(J)** The weight of *Grin2d*$^{f/ff}$ and *SMA-creER:Grin2d*$^{f/f}$ mice for gut system inspection. **(K)** The quantification for figure. S5I left. **(L)** The quantification for figure. S5J and K. (M) The quantification for figure. S5I right. **(N)** The fecal production of *Grin2d*$^{f/ff}$ and *SMA-creER:Grin2d*$^{f/f}$ mice in the 24hrs quarantine assay. **(O)** The appearance of *Grin2d*$^{f/ff}$ and *SMA-creER:Grin2d*$^{f/f}$ mice brain 45 min after evens blue injection. **(P)** The quantification for Figure. S5O. Data are presents as mean ± SEM.

Figure S6 **Ruan et al.,**

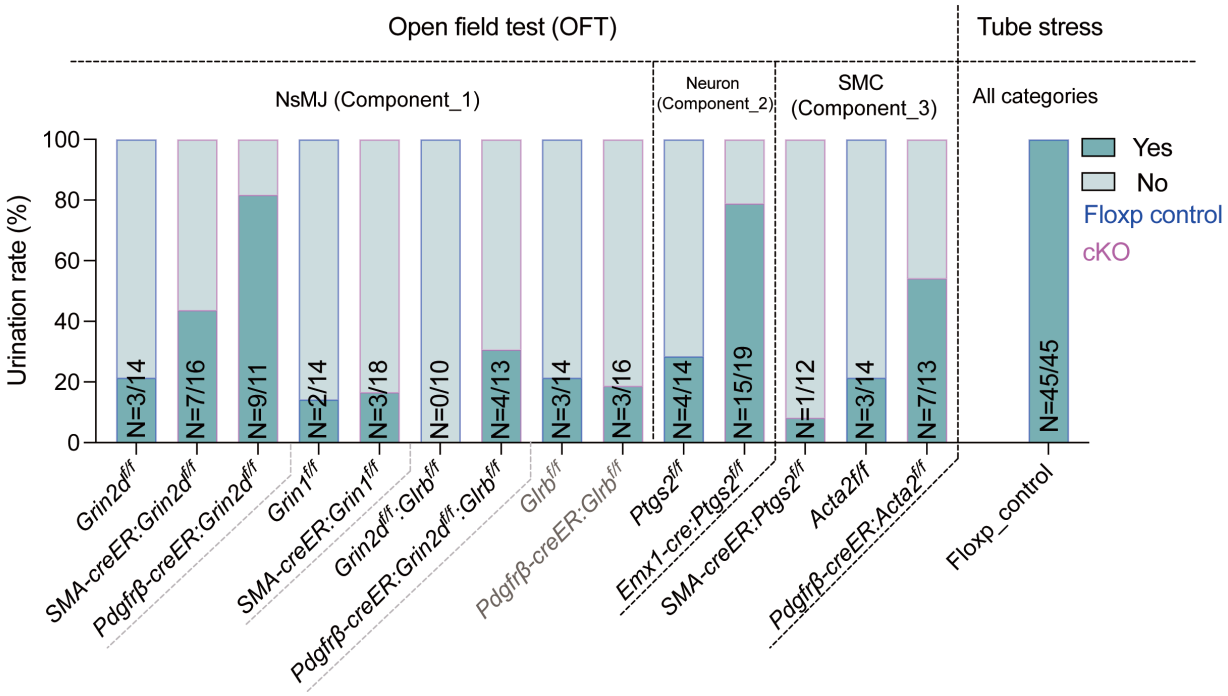

Fig. S6. The urination rates of each mouse line subjected to the assay of OFT_40*40 and that of all summed six floxed control lines subjected to acute tube stress.

Figure S7

Ruan et al.,

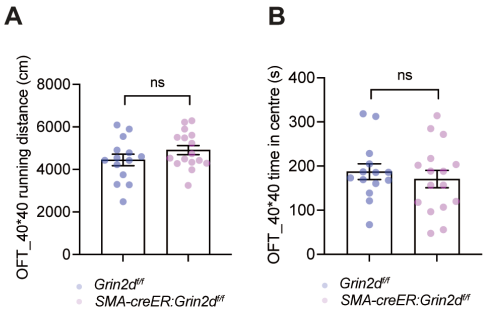

Fig. S7. The supplementary data of OFT. (A) The running distance of *Grin2d*$^{f/ff}$ and *SMA-creER:Grin2d*$^{f/f}$ mice in the OFT_40*40. **(B)** The time mice spent in the central area of the OFT_40*40 box during the test. Data are presents as mean ± SEM.

Figure S8

Ruan et al.,

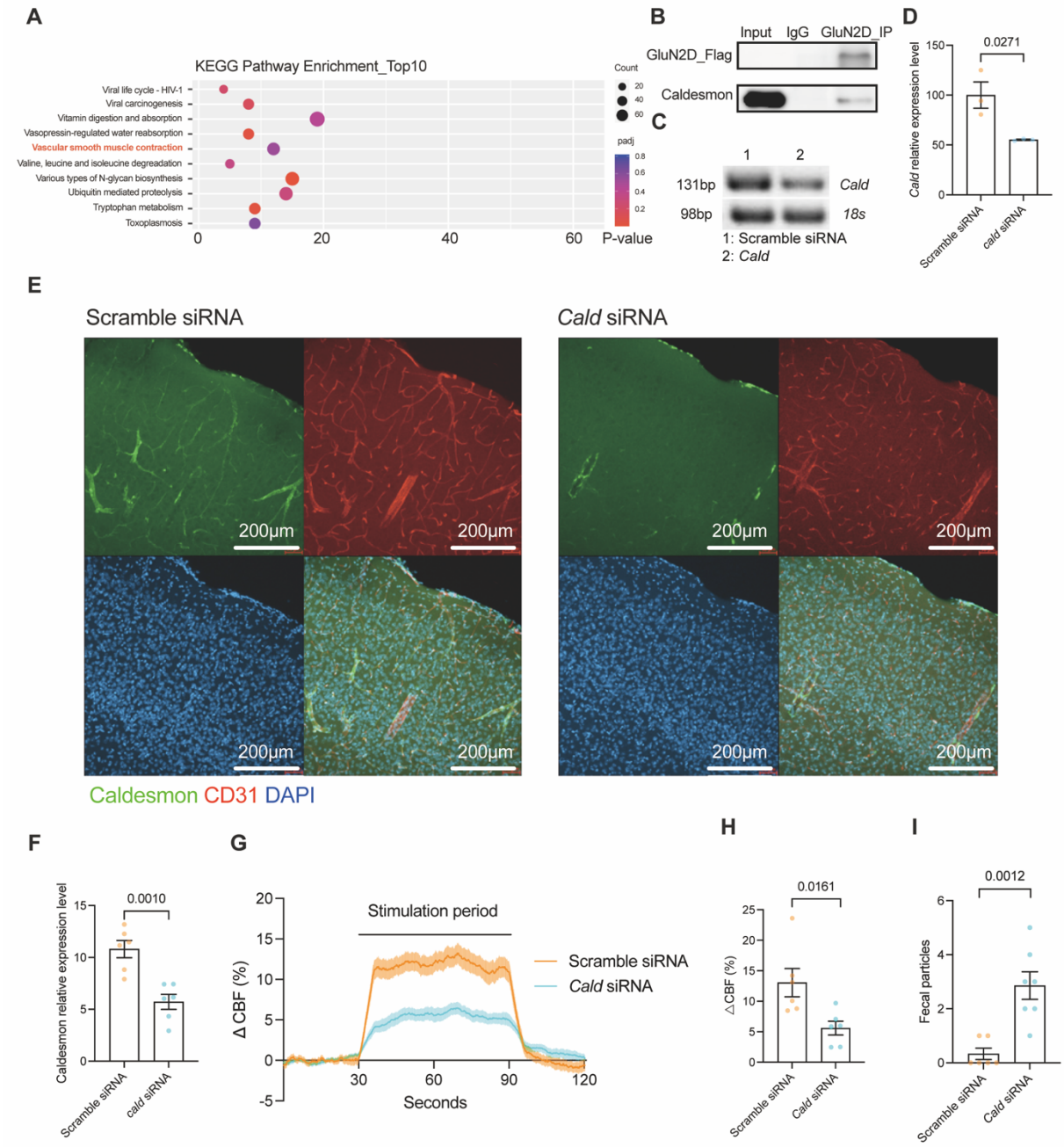

Fig. S8. The function of caldesmon in NVC for emotional regulation. (A) The top 10 KEGG pathways of proteins selected from immunoprecipitation products of GluN2D. **(B)** The detection of Caldesmon from the immunoprecipitation products of GluN2D. **(C)** The mRNA expression level of *Cald* in the cortex lysis with/without *Cald* siRNA interference. **(D)** The quantification for figure. S8C. **(E)** The immunofluorescence staining of Caldesmon and CD31 in the cortex of brain slices with/without *Cald* siRNA interference. **(F)** The quantification for figure. S8E. **(G)** CBF changes of mice with/without the *Cald* siRNA interference. **(H)** The quantification for figure. S8G. **(I)** The fecal production of mice in the OFT_40*40 with/without the *Cald* siRNA interference. Data are presents as mean ± SEM.

Figure S9

Ruan et al.,

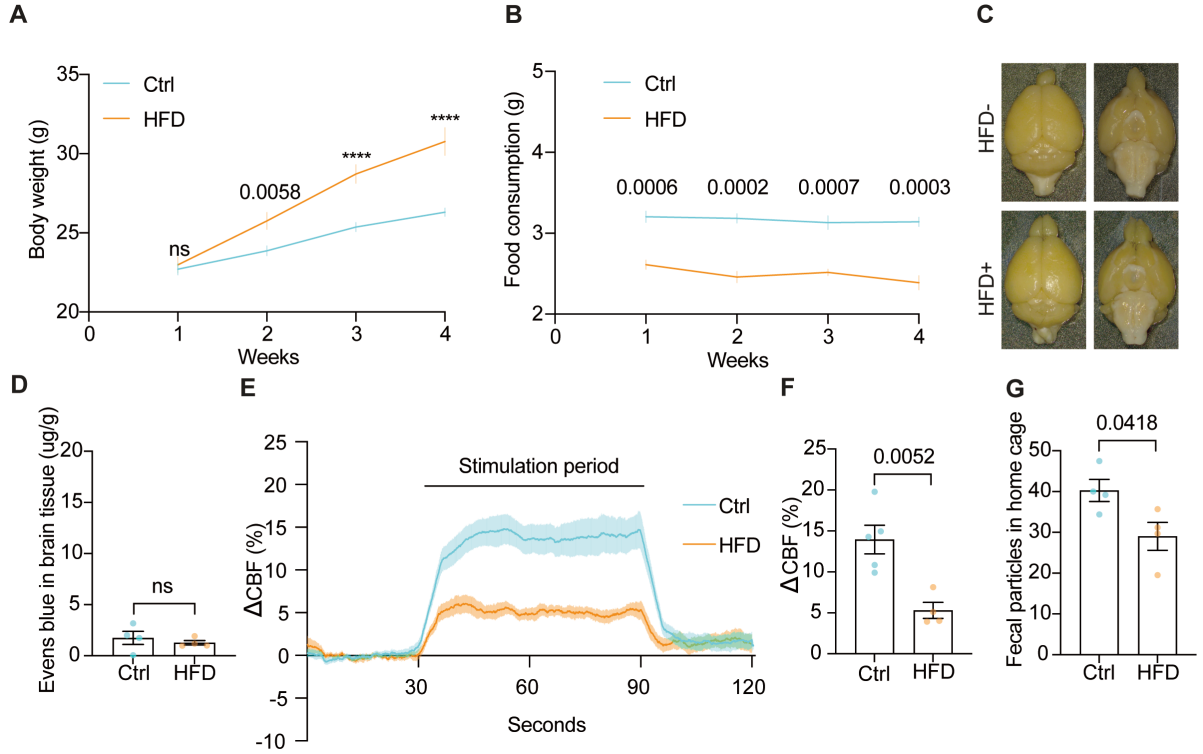

Fig. S9. The physical parameters inspection of HFD mice. (A) The weight of mice with/without HFD challenge. **(B)** The food consumption of mice with/without HFD challenge. **(C)** The appearance of mice brain with/without the HFD challenge 45 min after evens blue injection. **(D)** The quantification for figure. S9C. **(E)** CBF changes of mice with/without the HFD challenge during the whisker stimulation. **(F)** The quantification for figure. S9E. **(G)** The fecal production of mice with/without HFD challenge in the home cage per 24 hours. Data are presents as mean ± SEM.

Figure S10

Ruan et al.,

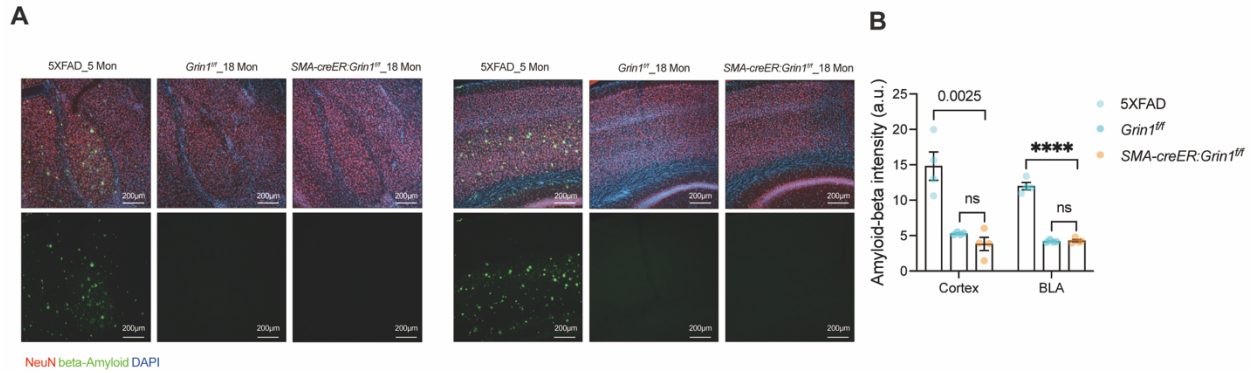

Fig. S10. The amyloid-β accumulation in chronic NVC-deficient mice. (A) The amyloid-beta plaque accumulation in the BLA (left) and cortex (right) of 5XFAD mice and 18-monts-old *Grin2d*$^{f/ff}$ and *SMA-creER:Grin2d*$^{f/f}$ mice. **(B)** The quantification for figure. 10A. Data are presents as mean ± SEM.

Figure S11

Ruan et al.,

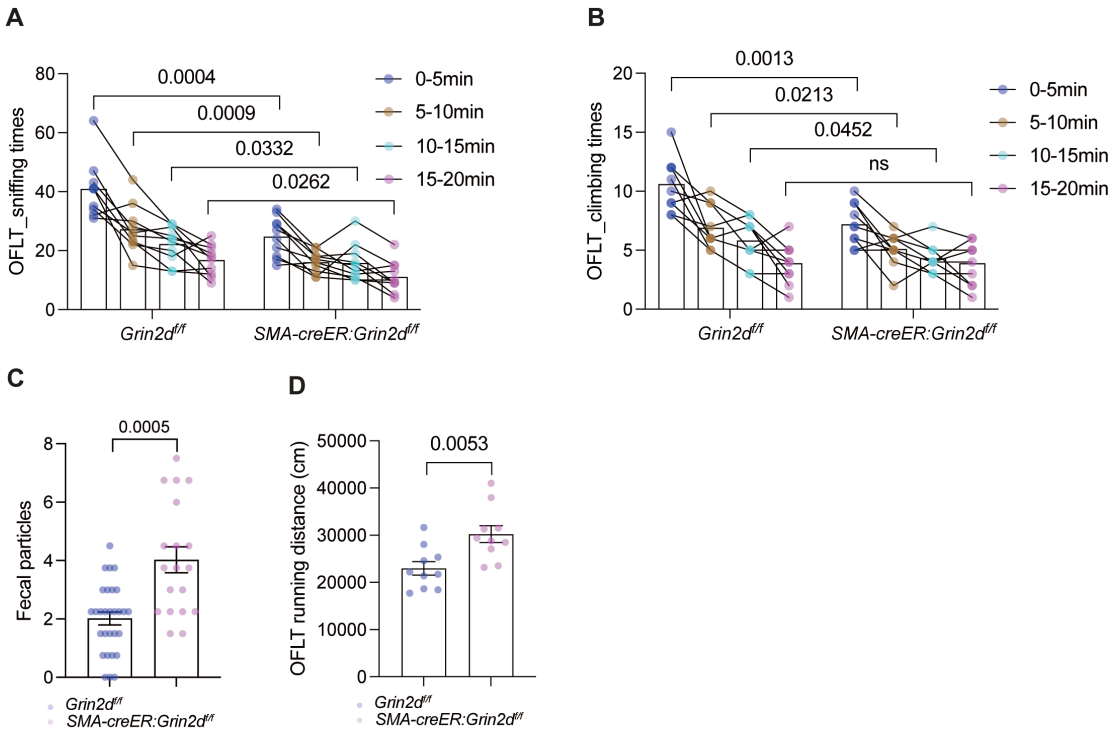

Fig. S11. The supplementary data of the OFLT. (A) The sniffing times of *Grin2d*$^{f/ff}$ and *SMA-creER:Grin2d*$^{f/f}$ mice to the metal fence during the OFLT. **(B)** The climbing times of *Grin2d*$^{f/ff}$ and *SMA-creER:Grin2d*$^{f/f}$ mice on the metal fence during the OFLT. **(C)** The fecal production of *Grin2d*$^{f/ff}$ and *SMA-creER:Grin2d*$^{f/f}$ mice during the OLFT. **(D)** The running distance of *Grin2d*$^{f/ff}$ and *SMA-creER:Grin2d*$^{f/f}$ mice in the OFLT. Data are presents as mean ± SEM.

Figure S12

Ruan et al.,

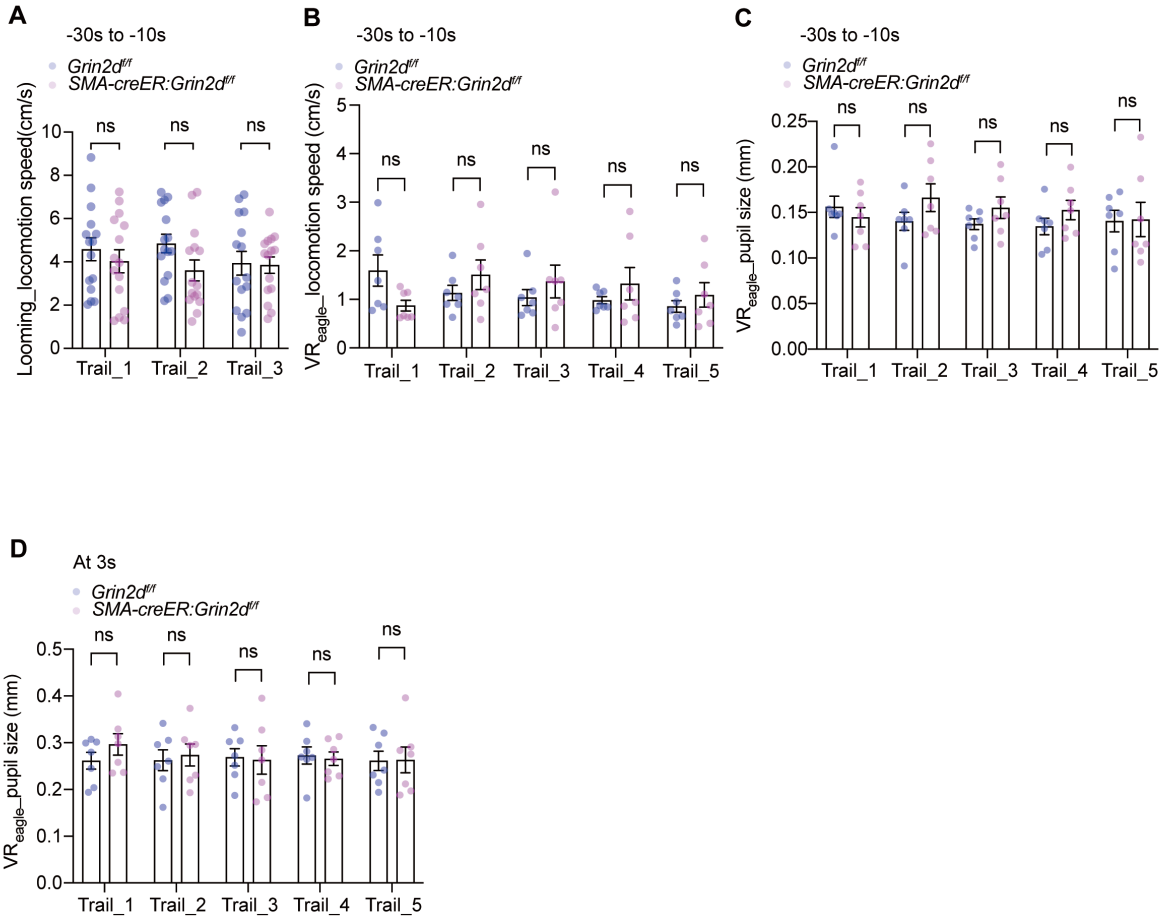

Fig. S12. The supplementary data of the looming assay and VR_{eagle} assay. (A) The locomotion speed of *Grin2d*$^{f/ff}$ and *SMA-creER:Grin2d*$^{f/f}$ mice from -30s to -10s in 3 trails of the looming assay. **(B)** The pupil size of *Grin2d*$^{f/ff}$ and *SMA-creER:Grin2d*$^{f/f}$ mice from -30s to -10s in 5 trails of the VR_{eagle} assay. **(C)** The locomotion speed of *Grin2d*$^{f/ff}$ and *SMA-creER:Grin2d*$^{f/f}$ mice from -30s to -10s in 5 trails of the VR_{eagle}. **(D)** The pupil size of *Grin2d*$^{f/ff}$ and *SMA-creER:Grin2d*$^{f/f}$ mice at 3s in 5 trails of the VR_{eagle} assay. Data are presents as mean ± SEM.

Figure S13

Ruan et al.,

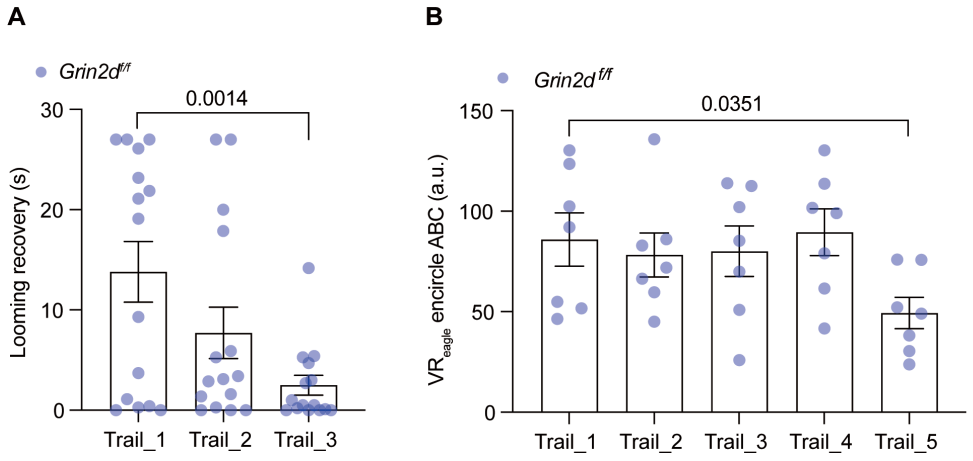

Fig. S13. The adaptation trend in the looming and VR_{eagle} assay. (A) The locomotion recovery latency of *Grin2d*$^{f/ff}$ mice in 3 trails of looming assay. **(B)** The normalized pupil size and locomotion encircle ABC of *Grin2d*$^{f/ff}$ mice in 5 trails of VR_{eagle} assay. Data are presents as mean ± SEM.

Figure S14

Ruan et al.,

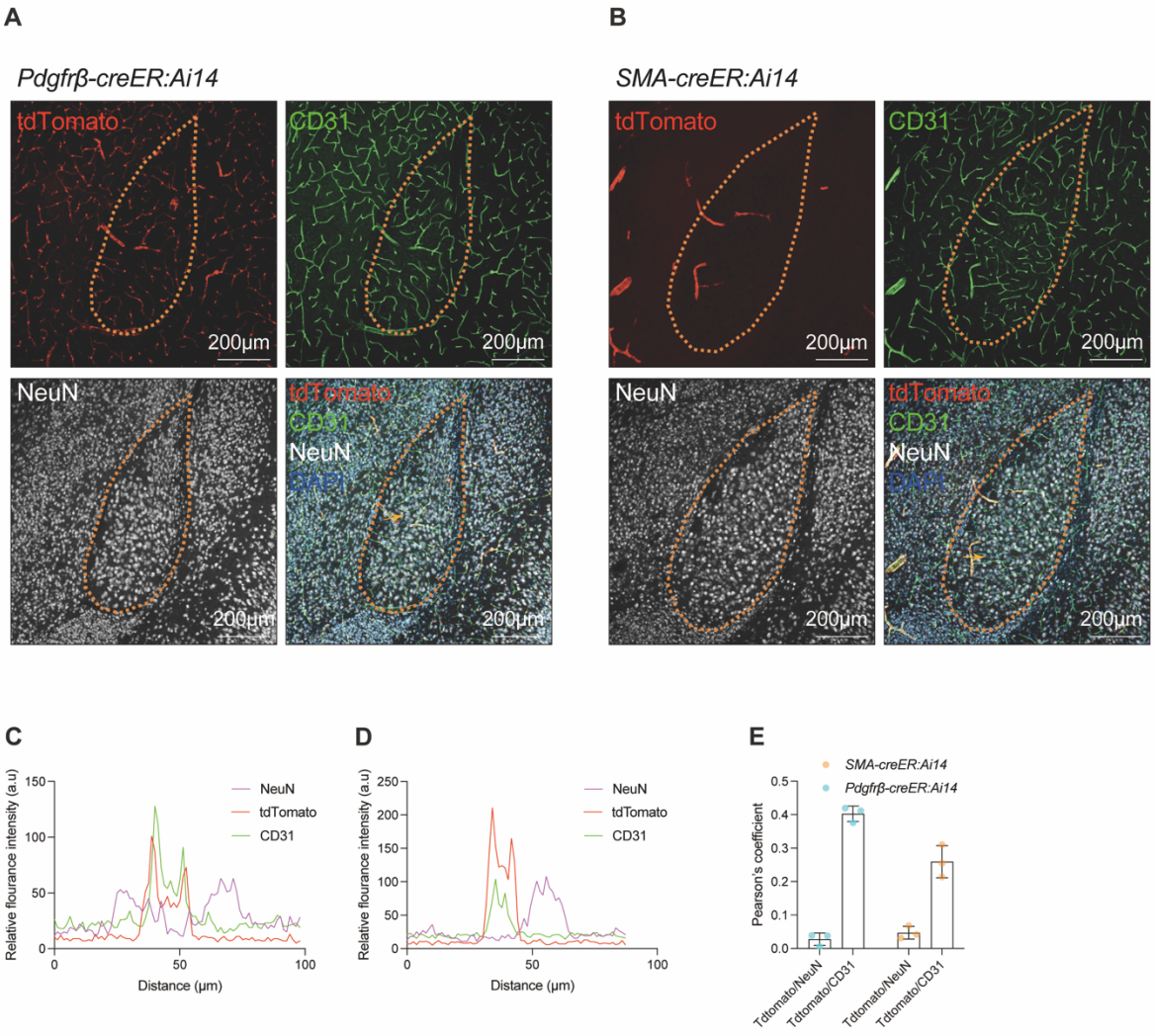

Fig. S14. The vasculature system distribution in BLA. (A) The tdotomato signal (driven by *Pdgfrβ-creER*) distribution pattern in the BLA. The yellow line marked the ROI for profile analysis. **(B)** The tdotomato signal (driven by *SMA-creER*) distribution pattern in the BLA. The yellow line marked the ROI for profile analysis **(C)** The line profile of signal distribution of figure. S14A. **(D)** The line profile of signal distribution of figure. S14B. **(E)** The quantification for of co-localization of tdtomato signal with CD31 and NeuN in figure. S14A and B. Data are presents as mean ± SEM.

Figure S15

Ruan et al.,

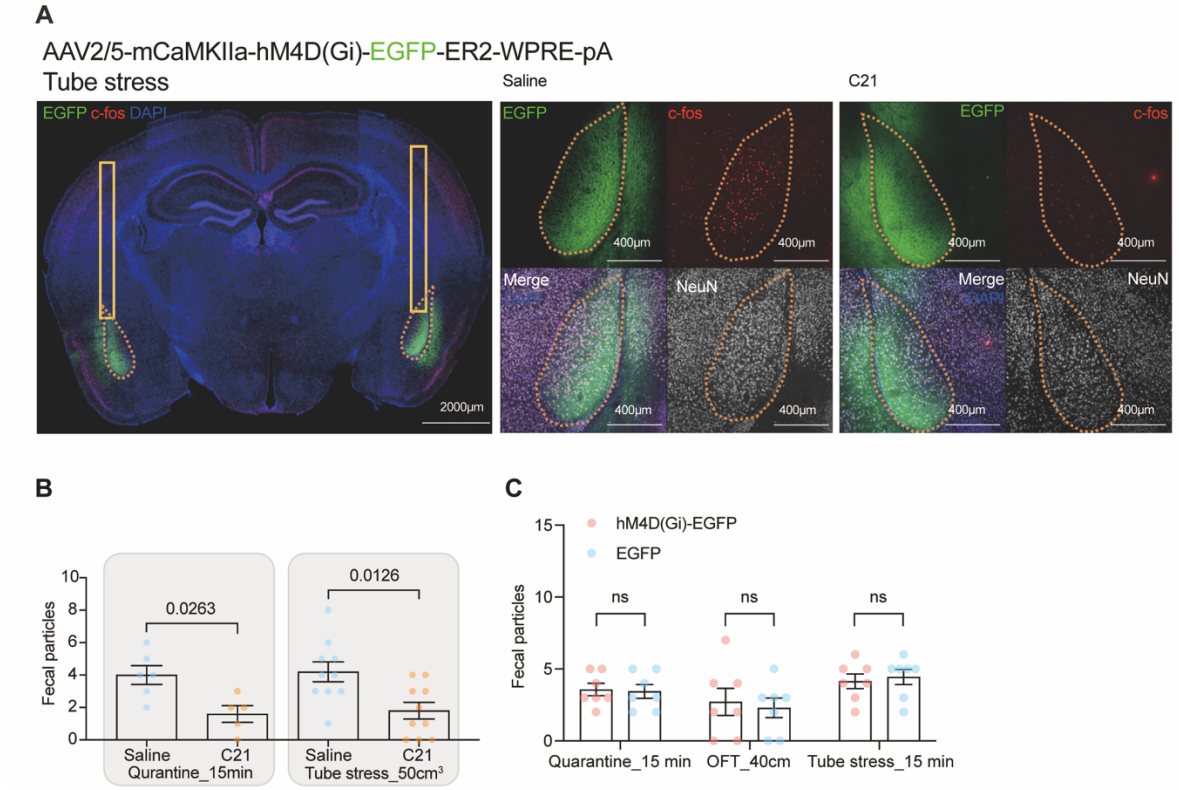

Fig. S15. The supplementary data of Figure. 4. (A) The schematic diagram brain slices of hM4D (Gi) injection in the BLA of mice. **(B)** The fecal production of *Grin2d*$^{f/f}$ mice injected hM4D (Gi) with/without C21 in the 15 min quarantine assay and 15 min acute tube stress (ARS). **(C)** The fecal particles of mice in different behavioral assays after overexpression of hM4D (Gi)-EGFP or EGFP in BLA by injection saline. Data are presents as mean ± SEM.

Table. S1. List of Mice Genetics

Common name	Strain name	Resource
Nestin-cre	B6.Cg-Tg(Nes-cre)1Kln/J	Yanmei Tao and Xu Hu, Hangzhou Normal University/ Southeast University
Emx1-cre	B6.129S2-Emx1$^{tm1(cre)Krj}$/J	Yanmei Tao and Xu Hu, Hangzhou Normal University/ Southeast University
SMA-cre^{ER}	Tg(Acta2-cre/ERT2)12Pcn	Bo Zhou, ShanghaiInstitutes for Biological Sciences, Chinese Academy of Sciences
Pdgfrβ-cre^{ER}	Tg(Pdgfrb-cre/ERT2)6096Rha	Xiang Yu, Peking University
Ai47	Gt(ROSA)26Sor$^{tm47(CAG-EGFP*)Hze}$	Zilong Qiu, Chinese Academy of Sciences Center for Excellence in Brain Science and Intelligence Technology, Chinese Academy of Sciences.
Ai14	B6.Cg-Gt(ROSA)26Sor$^{tm14(CAG-tdTomato)Hze}$/J	Woo-Ping Ge, Chinese Institute of Brain Research (CIBR)
Grin2d	B6/JGpt-Grin2d^{em1Cflox}/Gpt	GemPharmatech
Grin1	*Grin1*^{tm2Stl}	Yangang Sun, Chinese Academy of Sciences Center for Excellence in Brain Science and Intelligence Technology, Chinese Academy of Sciences
Ptgs2	C57BL/6JCya-Ptgs2^{em1flox}/Cya	Cyagen
Acta2	C57BL/6JGpt-Acta2^{em1Cflox}/Gpt	GemPharmatech
Glrb	C57BL/6JGpt-Glrb^{em1Cflox}/Gpt	GemPharmatech

Table. S2. List of Primer Pairs

Name		Sequence
Grin1	F	AAGAACCTGCAGCAGTACCA
	R	GCAGCAGGACTCATCAGTGT
Grin2a	F	TCAGGGACTTTGGAAAACGCT
	R	AAGTCATGCAGGGTTGGTTG
Grin2b	F	ACTAACTATCAATGAAGAACGGT
	R	CCAGACCCCAGAGTAACCA
Grin2c	F	TGTGGGCCTTCTTCGCTGTCATCT
	R	TGCCATTAGGTACCGTGCCAAAAC
Grin2d	F	TGGAGGAGTACGACTGGACAT
	R	CGCACTGACACTACGGAGC
Grin3a	F	CTGCACACCAGTCAGAGGTT
	R	TTCGTTGGTTGTCGTGACTC
Grin3b	F	TGGGGGTCTACCACTTGTCA
	R	TGGATCTTCTGGCTCGTGTG
Glrb	F	TTCAAAGGCATTCCTGTTGATGT
	R	TGAGCCTCTGAAGTCACTAGG
Cald	F	GCCGTTCAAGTGCTTCACTC
	R	TGTCAATCTTGGAGACTACTGCT
18s	F	CGGACACGGACAGGATTGACA
	R	CCAGACAAATCGCTCCACCAACTA
Cald (siRNA)	F	GUUUGAUCCGACCAUAACAGA
	R	UGUUAUGGUCGGAUCAAACUC

Table. S3. List of Antibodies

Name	Host	Cat#	Dilution	Company
Anti-NMDAR2D Antibody	Mouse	MAB5578	1:400 (IF) 1:2,500 (WB) 1:1,000 (IP)	Merck
Anti-Smoothelin antibody	Rabbit	ab219652	1:400 (IF)	abcam
α-Smooth Muscle Actin (ACTA2) Rabbit mAb	Rabbit	A17910	1:2,500 (WB)	ABclonal
Gephyrin Polyclonal Antibody	Rabbit	PA5-29036	1:400 (IF)	Invitrogen
BD Pharmingen™ Purified Rat Anti-Mouse CD31	Rat	557355	1:200 (IF)	BD
β-Amyloid (D54D2) XP® Rabbit mAb	Rabbit	D54D2	1:400 (IF)	CST
Anti-NeuN purified Antibody	Guinea Pig	ABN90P	1:800 (IF)	Merck
Anti-NMDAR1 Antibody, clone 54.1	Mouse	MAB363	1:400 (IF)	Merck
COX2/PTGS2 Rabbit pAb	Rabbit	A1253	1:400 (IF)	ABclonal
c-Fos antibody	Rabbit	226 003	1:1,000 (IF)	SYSY
Recombinant Alexa Fluor® 488 Anti-Caldesmon/CDM antibody	Rabbit	ab208116	1:400 (IF) 1:2,500 (WB)	abcam
Mice IgG	Mouse	A7028	1:1,000 (IP)	Beyotime
Donkey anti-Mouse IgG (H+L) ReadyProbes™ Secondary Antibody, Alexa Fluor™ 488	Donkey	R37114	1:1,000 (IF)	Invitrogen
Donkey anti-Rabbit IgG (H+L) ReadyProbes™ Secondary Antibody, Alexa Fluor™ 488	Donkey	R37118	1:1,000 (IF)	Invitrogen
Donkey anti-Rabbit IgG (H+L) Highly Cross-Adsorbed Secondary Antibody, Alexa Fluor™ 546	Donkey	A10040	1:1,000 (IF)	Invitrogen
Donkey anti-Rat IgG (H+L) Highly Cross-Adsorbed Secondary Antibody, Alexa Fluor™ 488	Donkey	A21208	1:1,000 (IF)	Invitrogen

Donkey anti-Rat IgG (H+L) Highly Cross-Adsorbed Secondary Antibody, Alexa Fluor™ 555	Donkey	A78945	1:1,000 (IF)	Invitrogen
Donkey anti-Rat IgG (H+L) Highly Cross-Adsorbed Secondary Antibody, Alexa Fluor™ Plus 647	Donkey	A48272	1:1,000 (IF)	Invitrogen
Alexa Fluor® 647 AffiniPure™ Donkey Anti-Guinea Pig IgG (H+L)	Donkey	706-605-148	1:1,000 (IF)	Jackson ImmunoResearch
β-Tubulin Mouse mAb	Mouse	AC021	1:5,000 (WB)	ABclonal
Goat Anti-Mouse IgG, HRP Conjugated	Goat	CW0102	1:10,000 (WB)	CWBIO
Goat Anti-Rabbit IgG, HRP Conjugated	Goat	CW0103	1:10,000 (WB)	CWBIO

Movie. S1. The diagram of Cat_{movie} assay (2X speed).

Movie. S2. The diagram of VR_{eagle} assay (2X speed).